Interaction of coherent phonons with defects and elementary excitations

2010 J. Phys.: Condens. Matter 22 073201

(http://iopscience.iop.org/0953-8984/22/7/073201)

J. Phys.: Condens. Matter **22** (2010) 073201 (23pp) doi:10.1088/0953-8984/22/7/073201

TOPICAL REVIEW

Interaction of coherent phonons with defects and elementary excitations

Muneaki Hase[1,2] **and Masahiro Kitajima**[3,4]

[1] Institute of Applied Physics, University of Tsukuba, 1-1-1 Tennodai, Tsukuba 305-8573, Japan
[2] PRESTO, Japan Science and Technology Agency, 4-1-8 Honcho, Kawaguchi, Saitama 332-0012, Japan
[3] Department of Applied Physics, School of Applied Science, National Defense Academy of Japan, Hashirimizu 1-10-20, Yokosuka, Kanagawa 239-8686, Japan

E-mail: mhase@bk.tsukuba.ac.jp and kitaji@nda.ac.jp

Received 13 October 2009, in final form 7 December 2009
Published 2 February 2010
Online at stacks.iop.org/JPhysCM/22/073201

Abstract

We present an overview of the feasibility of using coherent phonon spectroscopy to study interaction dynamics of excited lattice vibrations with their environments. By exploiting the features of coherent phonons with a pump–probe technique, one can study lattice motions in a sub-picosecond time range. The dephasing properties tell us not only about interaction dynamics with carriers (electrons and holes) or thermal phonons but also about point defects in crystals. Modulations of the coherent phonon amplitude by more than two modes are closely related to phonon–carrier or phonon–phonon interferences. Related to this phenomenon, formation of coherent phonons at higher harmonics gives direct evidence for phonon–phonon couplings. A combined study of coherent phonons and ultrafast carrier response can be useful for understanding phonon–carrier interaction dynamics. For metals like zinc, nonequilibrium electrons may dominate the dynamics of both relaxation and generation of coherent phonons. The frequency chirp of coherent phonons can be a direct measure of how and when phonon–phonon and phonon–carrier couplings occur. Carbon nanotubes show some complicated behavior due to the existence of many modes with different symmetries, resulting in superposition or interference. To illustrate one of the most interesting applications, the selective excitation of specific phonon modes through the use of a pulse train technique is shown.

(Some figures in this article are in colour only in the electronic version)

Contents

[4] Author to whom any correspondence should be addressed.

1. Introduction; generation process and decoherence

Phonons, having a wide variety of frequencies and wavevectors, propagate in solids with a density function $n(\omega)$ given by the Planck distribution $n(\omega) = [\exp(\frac{\hbar\omega}{kT}) - 1]^{-1}$ for thermally excited phonons. In this case, oscillatory phases of the phonons are completely random. Thus, individual oscillatory motions are canceled out by each other and, as a result, coherent macroscopic polarization will not appear. Such thermal lattice vibrations are called incoherent phonons and can be studied by frequency-domain spectroscopies such as Raman scattering (RS) and infrared (IR) absorption.

Irradiating a solid surface with ultrashort laser pulses will make the random phonons oscillate in phase. The coherent excitation of phonons is a general phenomenon occurring whenever ultrashort laser pulses interact with solids. A necessary condition to produce coherent phonons is the availability of Raman-active phonons and a pulse duration less than the oscillation period of the phonons. Such coherent lattice motions induce macroscopic changes in reflectivity or transmission, which are detected as coherent responses to the impulsive excitation by time-domain spectroscopies. The first observation of coherent phonons was reported by Nelson on dielectrics, in 1979 [1]. Since that time, coherent phonons have been measured in a wide variety of solids such as semiconductors [2–6], metals/semimetals [7–13], density wave compounds [14–16] and high-T_c superconductors [17–19]. Coherent phonons at surfaces can also be observed by transient second harmonic generation (SHG) techniques [20–22]. Using sub-10 fs laser pulses enables one to observe the high frequency coherent C–C stretching modes in carbon materials, such as carbon nanotubes (CNT) and diamonds [23–28].

Several mechanisms have been proposed for the generation of coherent phonons which explain well the properties of coherent optical phonons in a phenomenological manner. In transparent materials, the mechanism for coherent phonon generation was ascribed to impulsive stimulated Raman scattering (ISRS) [29]. To explain the behavior of coherent phonons in opaque materials, another mechanism, called the displacive excitation of coherent phonons (DECPs) mechanism [9], was proposed. For the latter case, instantaneous electronic excitation leads to a sudden change in the equilibrium position of the lattice, which responds by moving towards a new equilibrium position.

Following recent developments in femtosecond laser technologies, phonon modes in most crystals can now be observed. General aspects of this topic, including measuring techniques, coherent phonon properties (e.g., initial phase and dephasing) and generation (or relaxation) mechanisms, have been reviewed [30–32].

Thus, coherent phonon spectroscopy has entered its maturity. So far, the main objective in most studies has been to detect phonon modes with different symmetries in the time domain or to elucidate generation mechanisms. In other investigations, the aim is to apply coherent phonon spectroscopy to explore new physics or to manipulate collective lattice motions. Direct observations of phonon amplitude modulation in the time domain would make it possible to study interference between quasiparticles in solids. A combined study with carrier dynamics would provide information about the dynamics of electron–phonon couplings. The quantum kinetics of phonons in the ultrafast time domain could also be explored in principle [33, 34]. Understanding and even controlling material dynamics for such phenomena as phase transitions of solids or chemical reactions could become possible using techniques such as high-density laser excitation or multiple pulse irradiation. With information about the dephasing of coherence one could examine the dynamics of carrier–phonon interference and the scattering of phonons by defects.

It is a key issue to know how electron–hole carriers excited by laser irradiation lose energy and momentum in the first several to 10 femtoseconds (fs) and finally couple with phonons in solids. The dynamics of electron–phonon interactions is a common issue needed to understand and control material dynamics as well as to elucidate generation and relaxation mechanisms. As the major part of this review we will explain how electron–phonon interactions can be studied using coherent phonon spectroscopy. Phonon–phonon and phonon–defect interactions will also be discussed to help understand environmental effects on the coherent phonons. We will mainly show recent developments concerning electron and phonon dynamics in bulk materials such as metals, semiconductors and ferroelectrics. Such dynamical properties are important also for nanomaterials, and some recent results on carbon nanotubes will be described.

2. Scattering processes

2.1. Phonon–defect scattering

In semiconductors, carriers are scattered by lattice defects [35], such as vacancies, dislocations and impurities. Likewise, phonons are also scattered by the potential fluctuation of the periodic lattice due to defects; see figure 1. Owing to the presence of lattice defects, the phonons become 'localized modes', which can be described by a wavepacket motion of atomic vibrations. Effects of lattice defects on the properties of phonons are usually observed as changes in their frequency [36], damping and intensity (amplitude). In Raman scattering a spatial correlation model is widely used to describe the lineshape of Raman spectra, in which the wavefunction of a phonon is modified due to the confinement of the waves [36]. This is thought to be a pure dephasing process due to elastic scattering of coherent phonons caused by perturbations in the local potential by defects. Phase shifts to the wavefunction are induced in a random fashion, like $\propto \frac{1}{r}\sin(kr + \delta)$ [37], where r denotes the radius of the scattering spherical region, δ is the phase shift and $k = |\mathbf{k}|$. We next consider defects introduced by ion implantation into a crystal. In this case the combined scattering rate τ_{total} can be expressed as [38]

$$\frac{1}{\tau_{\text{total}}} = \frac{1}{\tau_{\text{anharmonic}}} + \frac{1}{\tau_{\text{defect}}}, \tag{1}$$

where $\tau_{\text{anharmonic}}$ is the anharmonic decay time and τ_{defect} is the phonon–defect scattering time constant, which depends on

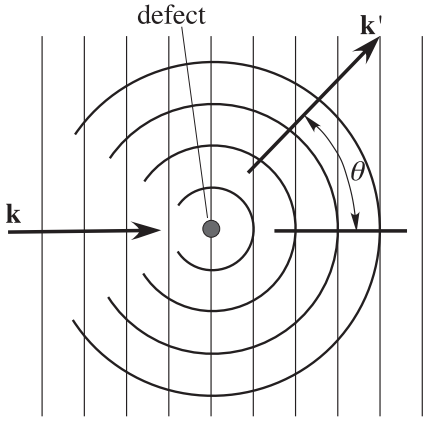

Figure 1. Schematic of phonon–defect scattering; scattering of an incident phonon of wavevector **k** by a defect. The scattered wave is spherical and the wavevector **k**′ represents a set of transitions from **k** to **k**′. θ is the angle between **k** and **k**′.

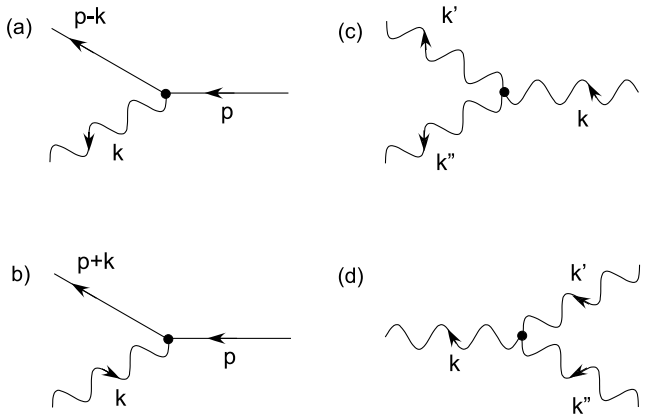

Figure 2. Carrier–phonon and phonon–phonon scattering processes. (a) Electron–phonon scattering, in which an electron emits a phonon. (b) Electron–phonon scattering in which an electron absorbs a phonon. (c) Phonon–phonon scattering, in which a phonon decays into two phonons. (d) Phonon–phonon scattering, in which two phonons generate a phonon.

the density of impurities introduced by ion implantation. The second term in equation (1) can be expressed as

$$\frac{1}{\tau_{\text{defect}}} = \gamma(\phi) = N_v(\phi)\sigma v, \tag{2}$$

where N_v is the number density of vacancies per unit volume as a function of ion fluence ϕ, σ is the cross section of a single vacancy and v is the frequency-dependent group velocity of the phonon in the long wavelength limit [39]. Equation (2) gives the rate at which coherent phonons are scattered by point defects or vacancies and lose their coherence.

2.2. Phonon–carrier scattering

It is clear that phonons in solids (e.g. metals) are modified by electron screening effects of the lattice potential. This potential correlation enters the electron Hamiltonian and gives a coupling between electrons and phonons. It is possible to solve the electron–phonon problem and obtain eigenstates of the electron–phonon system, although the theoretical part is beyond the scope of this paper. The most important carrier–phonon scattering in semiconductors occurs if charge carriers interact with the electric polarization induced by the relative displacement of positive and negative ions. In fact, in perfect crystals of polar semiconductors, such as GaAs, InP and GaN, carrier scattering at room temperature is governed by polar optical phonon scattering, which is generally named the Fröhlich interaction [40]. Acoustic or optical deformation potential interaction is another candidate for the effective carrier–phonon scattering mechanism found in non-polar semiconductors, such as Si and Ge [40].

For the case of the Fröhlich interaction, the Fröhlich Hamiltonian can be expressed by [40]

$$H_{\text{Fr}} = \mathrm{i}\sqrt{\frac{2\pi\hbar\omega_{\text{LO}}}{NV}(\epsilon_\infty^{-1} - \epsilon_0^{-1})}\sum_{\mathbf{k}}\frac{1}{k}[a_{\mathbf{k}}^\dagger \mathrm{e}^{\mathrm{i}\mathbf{k}\cdot\mathbf{r}} - a_{\mathbf{k}}\mathrm{e}^{\mathrm{i}\mathbf{k}\cdot\mathbf{r}}], \tag{3}$$

where ω_{LO} is the LO phonon frequency, N is the number of unit cells, V is the unit volume, ϵ_∞ and ϵ_0 are, respectively, the high and low frequency dielectric constants, $a_{\mathbf{k}}^\dagger$ and $a_{\mathbf{k}}$ are, respectively, the phonon creation and annihilation operators, **k** is the wavevector and **r** is the position vector. Thus, the Fröhlich Hamiltonian includes phonon creation and annihilation operators, indicating that the electron–phonon scattering can be considered as a process in which an electron emits or absorbs a phonon according to the energy and momentum conservation rules shown in figures 2(a) and (b) [41].

2.3. Phonon–phonon scattering

Phonon–phonon scattering is a manifestation of the anharmonic terms in the lattice potential. The crystal potential can be expanded in powers of the displacements of the ions from their equilibrium positions giving a sum in which the cubic and higher-order terms represent the anharmonicity. The anharmonic terms give an interaction between phonon modes and, as a result, the decay of a phonon into other phonon modes becomes possible. A few examples are listed in figures 2(c) and (d), where a phonon decay into two phonons or two phonons generates a phonon due to anharmonic interaction; see figure 3 [41]. Another manifestation of the anharmonic phonon–phonon coupling is the occurrence of higher harmonic phonons, whose oscillation can classically be expressed by

$$X(t) = A_0\cos(\omega_0 t) + A'\cos(2\omega_0 t) + A''\cos(3\omega_0 t) + \cdots, \tag{4}$$

where ω_0 is the fundamental frequency of a phonon mode, and A_0, A' and A'' are the amplitudes of the fundamental frequency and higher harmonics.

3. Experimental methods and results

The light source used in the examples presented in this review was a mode-locked Ti:sapphire laser with a central

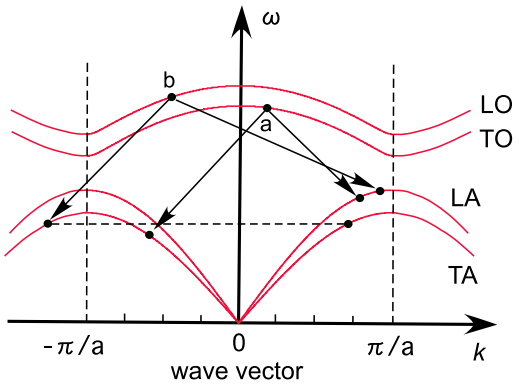

Figure 3. Anharmonic phonon decay processes. The TO phonon (a) decays into LA and TA phonons, while the LO phonon (b) decays into LA and TA phonons at slightly different wavevectors. The horizontal broken line represents the umklapp process, where the wavevector of the TA phonon is created outside the first Brillouin zone.

wavelength of either 800 or 400 nm and pulse width of <10–100 fs, depending on the phonon modes and optical/electronic properties of the samples. A standard reflection-type pump–probe configuration (figure 4(b)) was employed in the case of metals and ferroelectric materials. Pump and probe beams were polarized orthogonal to each other to avoid interference from the scattered pump beam, and were focused to a diameter of 30–70 μm on the samples. The isotropic transient reflectivity (TR) change $\Delta R/R$ was measured as a function of the delay time by scanning the optical path length of the probe beam. To detect polar or not-totally symmetric phonon modes, the electro-optic (EO) reflectivity change ($\Delta R_{eo}/R$) was measured (figure 5) [31]. In the EO sampling mode the difference in the reflectivity was measured, enabling cancellation of the isotropic carrier (or phonon) contributions from the signals.

3.1. Phonon–defect scattering in semimetals and semiconductors

3.1.1. Enhancement of phonon dephasing in Bi. We first show the phonon dynamics on ion-irradiated bismuth (Bi) films. Currently, Bi is used as a model sample to explore new physics with coherent phonon spectroscopy because it produces extremely high signals (large phonon amplitude). Ten pieces of polycrystalline bismuth films were prepared by evaporation onto polished Si(001) substrates at the same time in a vacuum chamber. They were about 500 nm thick, and x-ray diffraction measurements showed that they were polycrystalline with the same quality. In order to examine the effect of ion irradiation, 500 keV Bi^+ ions were implanted into the polycrystalline films at doses from 1×10^{14} Bi^+ cm^{-2} to 2×10^{15} Bi^+ cm^{-2} (see figure 4(a)). The damage depth deduced by a Monte Carlo calculation (TRIM) was about 200 nm [42] and the damage profile was close to a Gaussian function with a peak at 43 nm from the surface as shown in figure 6. The femtosecond measurements were performed at room temperature. The penetration depth of the laser beam is about 130 nm, which extends into the irradiation damage region.

The coherent phonon signal from all of the Bi films confirmed that there was no difference in the dephasing time of the coherent phonon between the ten Bi films before the ion irradiation. As shown in figure 7(a), coherent oscillations of the fully symmetric A_{1g} mode are observed for the ion-implanted bismuth films. In this figure, in order to estimate the decay time τ of the coherent A_{1g} mode for various doses, the time derivatives of the reflectivity change are taken. The τ is obtained by fitting the time-domain data to a damped harmonic oscillation with a single exponential decay, and the values of τ for the coherent A_{1g} mode are shown in figure 7(a) for various doses. The decay time gradually decreased from 3.86 to 2.39 ps as the dose increased, being clearly seen with the guide envelopes of a single exponential decay. This effect can be qualitatively explained by phonon scattering from defects created by ion implantation.

Figure 7(b) shows the decay rate of the coherent A_{1g} mode obtained from the inverse of the decay time deduced by the curve fitting. The decay rate increases almost linearly with increasing ion dose as shown by a solid line. The dephasing process of the coherent optical phonons in solids has been considered to be an anharmonic decay due to phonon–phonon interactions in **k**-space [43, 44]. This decay process depends mainly on lattice temperature. The result of the dose dependence (see figure 7(b)) shows clearly that another

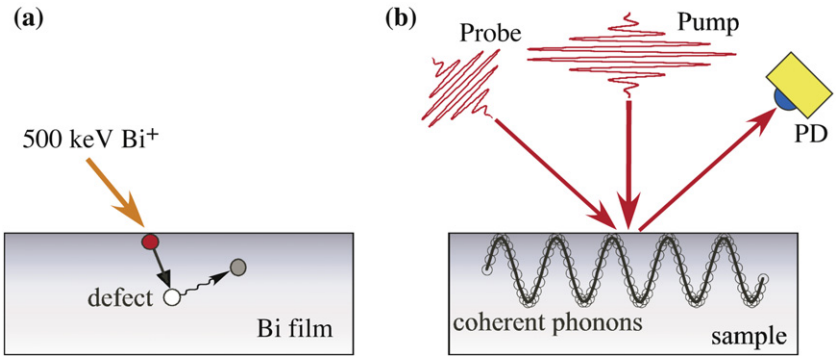

Figure 4. Experimental techniques. (a) Bi^+ ion irradiation into Bi thin films to introduce lattice defects. (b) Schematic of the pump–probe reflectivity measurement. The stronger pump pulse generates coherent phonons in solids, while the weaker probe pulse detects the change in the reflectivity through the photodiode (PD).

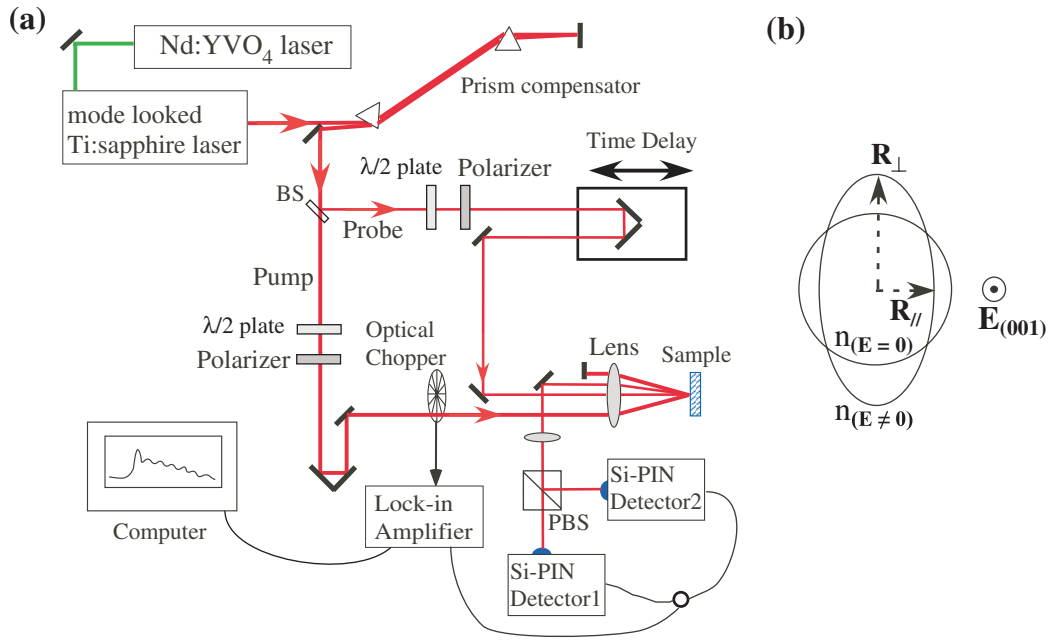

Figure 5. Experimental techniques used for the case of GaAs. (a) Pump–probe optical set-up based on electro-optic (EO) sampling mode. (b) EO reflectivity change induced by the light field (**E**) on the (001) surface, which is detected by the difference in the reflectivity between $R_\perp$ and $R_\parallel$.

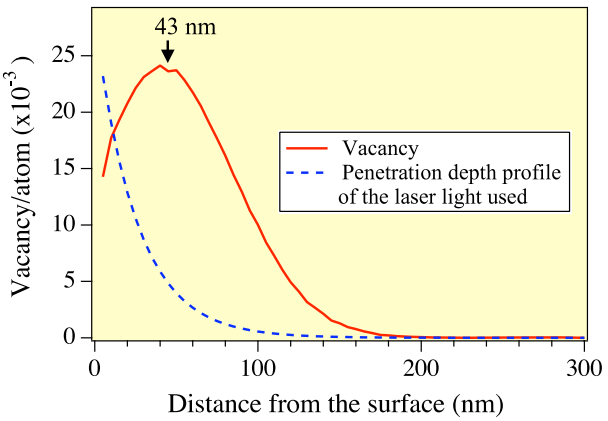

Figure 6. The damage profile of the Bi film with Bi^+ ion irradiation, compared with the penetration depth profile of the femtosecond laser used in the experiment.

effective scattering event for the phonon dephasing process is phonon–defect scattering.

Based on the assumption that the anharmonic decay process would not be affected by the existence of defects, the experimental data in figure 7(b) can be fitted with equation (1) and we obtained $\tau_{\text{anharmonic}} = 3.86$ ps as a constant. The value of $\tau_{\text{anharmonic}}$ almost agrees with that obtained for the as-grown Bi films (3.57 ps) in our measurements. The amplitude of the coherent phonon oscillation obtained at the dose of 2×10^{15} Bi^+ cm^{-2} was smaller than those of others by a factor of 0.8. This decrease of the amplitude for the highly ion-implanted Bi would be due to an initial damping of the coherent phonons.

According to the spatial correlation model previously used in the analysis of Raman data, the effect of disorder is observed as the asymmetric broadening of the Raman band that originates from the relaxation of the wavevector selection rule [36]. In our time-domain experiment, the bandwidth of the Fourier-transformed (FT) spectra for the A_{1g} mode was slightly broader for only the highly ion-implanted Bi film than that for the as-grown film. However, the asymmetric lineshape of the coherent A_{1g} mode was not clearly observed for the FT spectra. A possible reason for this result is that the $\mathbf{k} = 0$ phonons are mainly observed by the coherent phonon measurement in opaque materials [30]. The intensity of Raman spectra obtained for the Bi films ion-implanted at the same dose were very weak, and no difference was observed in the bandwidth of the Raman spectra in the frequency domain. Thus, coherent phonon measurement in the time domain is of great advantage to study dephasing of phonons directly.

3.1.2. Effect of lattice defects in GaAs. In the case of III–V compound semiconductors, there has been an intriguing application that converts a doped layer into a highly resistive one by ion irradiation of He^+ and other light particles [45]. However, a mechanism of the carrier removal by ion irradiation has not yet been fully understood by deep level transient spectroscopy (DLTS) [46] and by Raman scattering spectroscopy [47] because the deep level is too deep to be observed by DLTS and little is known about the information of relaxation dynamics of carriers. A pump–probe isotropic reflectivity measurement of carriers in semiconductors with ultrashort light pulses has enabled us to study the dynamics of photoexcited carriers, such as carrier–carrier scattering, carrier–phonon scattering and recombination of carriers [48]. Time-resolved measurements of carrier dynamics is needed in ion-irradiated semiconductors to understand how doped free carriers are trapped [49].

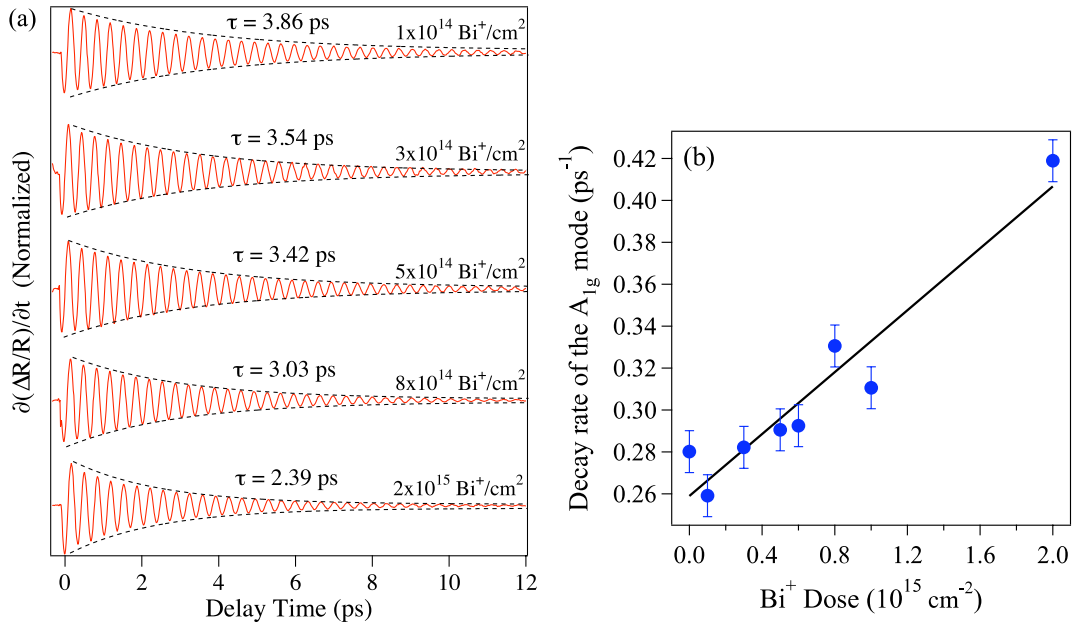

Figure 7. (a) The time derivatives of the TR signal. τ is the decay time of the coherent A_{1g} mode deduced by curve fitting with a damped harmonic oscillator. The dashed curve corresponds to the guide for a single exponential decay. (b) The decay rate of the coherent A_{1g} mode obtained by inverting the decay time τ as a function of Bi^+ dose. The solid line corresponds to the fit of the data with equation (1) using $\tau_{\text{anharmonic}} = 3.86$ ps.

Among compound semiconductors, GaAs is a promising material for device applications such as ultrafast optical switching [50] and terahertz radiation [31]. In low temperature (LT) grown GaAs, several groups found that the carrier lifetime decreased due to trapping of photo-generated carriers by As-precipitates, which was related to the deep levels below the conduction bands (CBs) [50–52]. The results suggest that carrier trapping due to the deep levels occurs on a timescale from 0.3 to 1.4 ps. In Si-doped n-type GaAs, it is well known that plasmons and LO phonons form coupled modes through Coulomb interactions (figure 8), and the frequencies of the LO phonon–plasmon coupled (LOPC) modes depend on the carrier density n_e according to the relation of the plasma frequency $\omega_p = \sqrt{4\pi e^2 n_e/\varepsilon_\infty \mu}$, where ε_∞ is the high frequency dielectric constant and μ is the reduced electron–hole mass [53, 54]. Recently ultrafast relaxation of the coherent LOPC modes in n-GaAs has been studied using pump–probe techniques and the frequency of the LOPC modes was determined by the total electron density, which results from both background doping and optical excitation [55, 56]. One can even obtain the carrier mobility values in GaAs from the relaxation times of the observed coherent LOPC modes [57]. Thus, the frequencies of coherent LOPC modes are sensitive to both doped- and photoexcited carrier densities, the latter of which cannot be observed by Raman scattering.

In this section, effects of He^+ irradiation on the coherent LOPC modes in n-GaAs are investigated using a femtosecond pump–probe technique. The coherent oscillations of the LOPC modes are found to be eliminated by means of He^+ irradiation, which is attributed to a decrease in the doped carriers caused by trapping via deep levels [58].

In the case of GaAs, the samples used were Si-doped n-GaAs with a doped carrier density of $n_{\text{dop}} = 1.4 \times 10^{18}$ cm^{-3}.

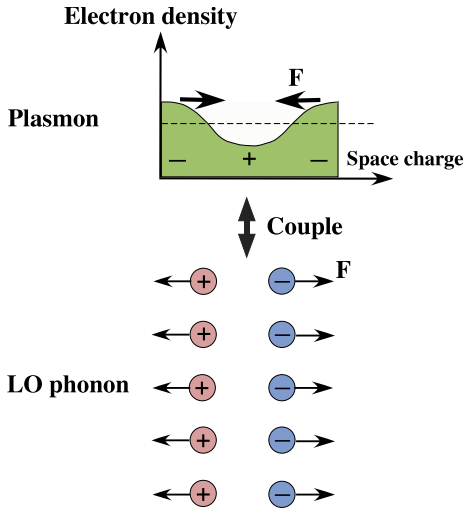

Figure 8. The coupling between the plasmon and the LO phonon through Coulomb interactions. **F** represents the Coulomb force.

They were irradiated with 5 keV He^+ at various doses from 9.4×10^{12} to 3.0×10^{13} He^+ cm^{-2} in an ultrahigh vacuum chamber. The damage profile was calculated by Monte Carlo calculations [42] to be a Gaussian with a peak at 30 nm from the surface and a width of 50 nm, which is comparable to the 90 nm penetration depth of the laser. The maximum photoexcited carrier density was estimated to be $n_{\text{exc}} = 5 \times 10^{17}$ cm^{-3} from the pump power density and the absorption coefficient.

The time derivatives of the EO reflectivity change ($\Delta R_{\text{eo}}/R$) for n-GaAs before and after He^+ irradiation are shown in figure 9(a). Coherent oscillations with strong mode-beating are clearly observed before ion irradiation. The mode-

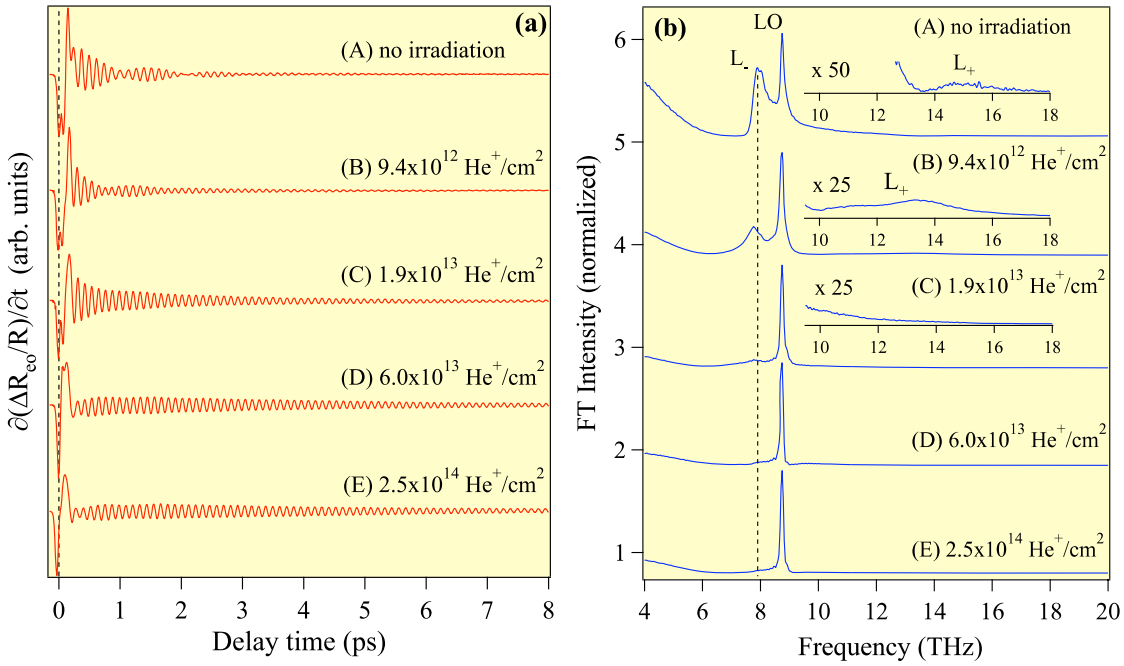

Figure 9. (a) The time derivatives of the EO signal for n-GaAs obtained at 300 K for various He^+ doses. (b) FT spectra obtained from time-domain data in (a). The dotted line shows the peak frequency of the TO mode for the unirradiated sample, indicating that the L_- mode is located at almost the TO frequency because the L_- mode is phonon-like at $(n_{dop} + n_{exc}) \sim 2 \times 10^{18}$ cm^{-3}.

beating is due to the coexistence of the LO phonon (8.75 THz), and the lower (L_- at 7.91 THz) and upper (L_+ at 14.9 THz) branches of the LOPC modes [55, 59], as shown in the FT spectra in figure 9(b). The mode-beating almost disappears after ion irradiation at doses higher than 1.9×10^{13} He^+ cm^{-2}. The frequency of the LO mode is not changed by the ion irradiation, whereas those of the L_- and the L^+ modes shift from 7.91 down to 7.7 THz, and from 14.9 down to 13.6 THz, respectively, after an irradiation of 9.4×10^{12} He^+ cm^{-2}. The shifts of the LOPC mode frequencies suggest a decrease in the free carrier density of 3.5×10^{17} cm^{-3} after an irradiation of 9.4×10^{12} He^+ cm^{-2} given that the frequencies of the LOPC modes depend on the carrier density [53]. This suggests that single vacancies are responsible for the trapping of photoexcited carriers in He^+ irradiated GaAs. Both the L_- and the L_+ modes in the FT spectra almost disappear at 1.9×10^{13} He^+ cm^{-2}, corresponding to the disappearance of mode-beating in the time domain. For doses $\geqslant 6.0 \times 10^{13}$ He^+ cm^{-2}, only the LO mode was observed.

The dephasing behavior of coherent phonons in the ion-irradiated GaAs is unexpected. The dephasing time of the LO phonon and the L_- mode are estimated by fitting the time-domain data with exponentially damped harmonic oscillations. The dephasing time of the LO phonon slightly increases from 2.1 to 3.0 ps after 3.0×10^{13} He^+ cm^{-2} irradiation. This is in contrast to the case of the ion-irradiated semimetal bismuth, in which the dephasing time of the coherent A_{1g} mode decreases with Bi^+ dose due to phonon–defect scattering (see section 3.1.1). A possible explanation for the slightly increased dephasing time of the LO phonon is a weakening of the electron–phonon scattering [47].

The dephasing time of the L_- mode decreases from 970 ± 40 to 340 ± 40 fs at 9.4×10^{12} He^+ cm^{-2}. In contrast, the dephasing time of the L_+ mode obtained by a time partitioning Fourier transform [59] increases from 100 ± 40 fs before irradiation to 150 ± 40 fs at 9.4×10^{12} He^+ cm^{-2}. The dephasing times of the coupled modes cannot be explained simply by defect scattering caused by deformation potential interaction from local strain around the defects, as this usually decreases the dephasing time [35]. The difference in the dephasing time of the LOPC modes suggests that the coupled modes change from a plasmon-like into a phonon-like mode for the L_+ mode and vice versa for the L_- mode [54].

Since deep levels are located below the donor levels [46], doped carriers as well as photo-generated carriers can be deeply trapped, both of which would affect the dephasing of the LOPC modes. In addition, there are enough single vacancies ($\approx 2 \times 10^{18}$ cm^{-3} at 9.4×10^{12} He^+ cm^{-2}) to trap almost all the doped carriers (1.4×10^{18} cm^{-3}). Therefore, the disappearance of the LOPC mode oscillations, as well as the dose dependence of the dephasing time of the coupled modes, appear to be due to the trapping of doped carriers [58].

3.1.3. Phonon–defect scattering in graphite. Graphite is a model two-dimensional system in solid-state physics and has many industrial applications. Carrier dynamics in graphite was studied by pump–probe TR measurements back in 1990, in which the photoexcited carriers were observed to equilibrate with the lattice and recombine within 1 ps [60]. The lattice vibration of graphite, however, was not observed directly in the time domain until the work by Mishina *et al* [61] a decade later. They discussed generation and detection mechanisms of coherent phonons by interlayer shear modes. Here we will

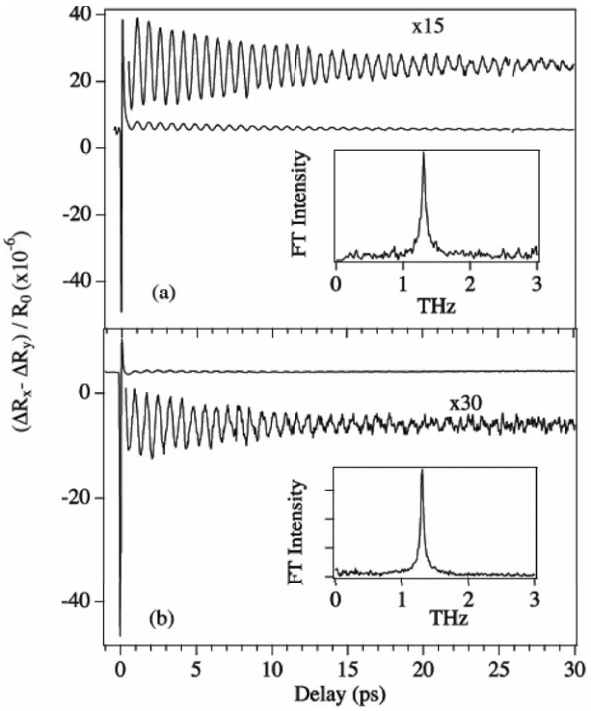

Figure 10. Time-resolved EO reflectivity change obtained for graphite before (a) and after irradiation with 8×10^{13} He^+ cm^{-2} (b). The insets show the Fourier transforms of the time-domain signals. Reproduced with permission from [39]. Copyright 2001 by the American Institute of Physics.

describe the dephasing dynamics of coherent phonons caused by defect scattering in graphite [39]. The samples used were highly oriented pyrolytic graphite (HOPG). Point defects were introduced by implanting the samples at room temperature with 5 keV He^+ in an ultrahigh vacuum chamber. The damage depth of the ions was large compared to the optical penetration depths of the 800 and 514.5 nm light used in the study. To estimate the number density of vacancies in the ion-irradiated HOPG samples, the relative intensities of the disorder-induced mode (D-peak) to the crystal mode (G-peak) of the in-plane C–C stretching mode [36] were measured with conventional Raman spectroscopy using 514.5 nm light.

Figure 10(a) shows the normalized $\Delta R_{eo}/R$ signal for unirradiated HOPG. The oscillation of the reflectivity has a frequency of 1.31 THz (42 cm^{-1}), as shown in the FT spectrum in the inset of figure 10(a), and corresponds to the coherent interlayer shearing (E_{2g1}) mode of graphite. The decay time of the coherent E_{2g1} phonon was $E_{2g1} = 11.6 \pm 0.9$ ps for unirradiated graphite, which is in agreement with previous work [61]. Upon ion irradiation, the amplitude of the coherent E_{2g1} phonon decreased as shown in figure 10(b). The coherent phonon frequency was almost constant, except for a slight redshift at very low fluences. The decay rate $\Gamma_{E_{2g1}} = 1/\tau_{E_{2g1}}$ increased with increasing ion fluence above 4×10^{13} He^+ cm^{-2}, similar to Bi (see figure 7(b)), while it was independent of the ion fluence below 4×10^{13} He^+ cm^{-2} [39]. The linear dependence with ion fluence was attributed to scattering of the coherent phonons by single point defects.

3.2. Phonon–carrier scattering in semiconductors, metals and low-dimensional systems

3.2.1. Silicon:destructive phonon–carrier interference. Study of coherent optical phonons in Si has revealed the ultrafast formation of renormalized quasiparticles [34]. Figure 11 shows an EO reflectivity change of n-doped Si(001) obtained by using a sub-10 fs pulse laser with an energy of 3.05 eV (400 nm wavelength). The excitation photon energy is close to the E_0' critical point, corresponding to the direct transition. The data show the coherent optical phonons to have a frequency of 15.3 THz; see figure 11(a). Rotation of the sample by 45° from the $\Gamma_{25'}$ to the Γ_{12} configuration leads to disappearance of the coherent oscillation, which suggests a phase shift (π) of the coherent phonons in the $R_\parallel$ and $R_\perp$ components, resulting in the cancellation of the oscillation with the Γ_{12} configuration. A similar polarization dependence was observed for the coherent optical phonons of Ge [62] and diamond [25]. In the time-dependent spectral amplitude (chronogram) plotted in figure 11(b), the optical phonon is seen as the horizontal band at 15.3 THz for $t > 0$. The chronogram also reveals a broadband response at $t \approx 0$ due to coherent electronic coupling of the pump and probe fields via nonlinear susceptibility. The most intriguing aspect of the chronogram is the antiresonance at 15.3 THz slightly after $t = 0$ (figures 11(b) and (c)). This reveals a Fano-type interference effect is generating the coherent phonons and subsequent 'dressing' by electron–hole pairs photoexcited near the Γ-point and along the Λ direction. A many-body time-dependent approach has recently shown that scattering caused by the deformation potential interaction is the origin of the destructive interference [63]. These results clearly demonstrate the possibility of observing quantum mechanical manifestations of carrier–phonon interactions in real time [64], which could previously only be deduced from transport measurements and spectral lineshape analysis. A similar signature of a Fano-type resonance appears near the time-zero region for coherent E_{2g} phonons in Zn under intense laser excitation, in which both the destructive (antiresonance) and constructive interference are observed [65].

The initial phase of the coherent optical phonons was found to be $\varphi \approx 20°$, when the excitation photon energy (3.05 eV) was close to the E_0' critical point [34], assuming a damped harmonic oscillation $\frac{\Delta R(t)}{R} \propto e^{-\Gamma t}\cos(\omega_0 t + \varphi)$. The initial phase was shifted to $\varphi \approx 90°$ when excited far below the direct bandgap with 1.55 eV photons [66]. The results indicated that the coherent oscillation is a sine function of time for non-resonant excitation but approaches a cosine function for near-resonant excitation. Based on these observations, Riffe and Sabbah [66] proposed a 'Raman scattering finite lifetime (RSFL)' model, in which the initial phase of the coherent phonons depends on the electronic relaxation rate γ:

$$\varphi_{RSFL} = \tan^{-1}\left[\frac{(\gamma - \Gamma)2\epsilon_2 + 4\pi^2\nu^2\epsilon_1'}{2\pi\nu(2\epsilon_2 - \gamma\epsilon_1')}\right] + \frac{\pi}{2}, \qquad (5)$$

where $\epsilon = \epsilon_1 + i\epsilon_2$ is the dielectric function at the laser frequency Ω_0, and $\epsilon_1' = d\epsilon_1/d\Omega$.

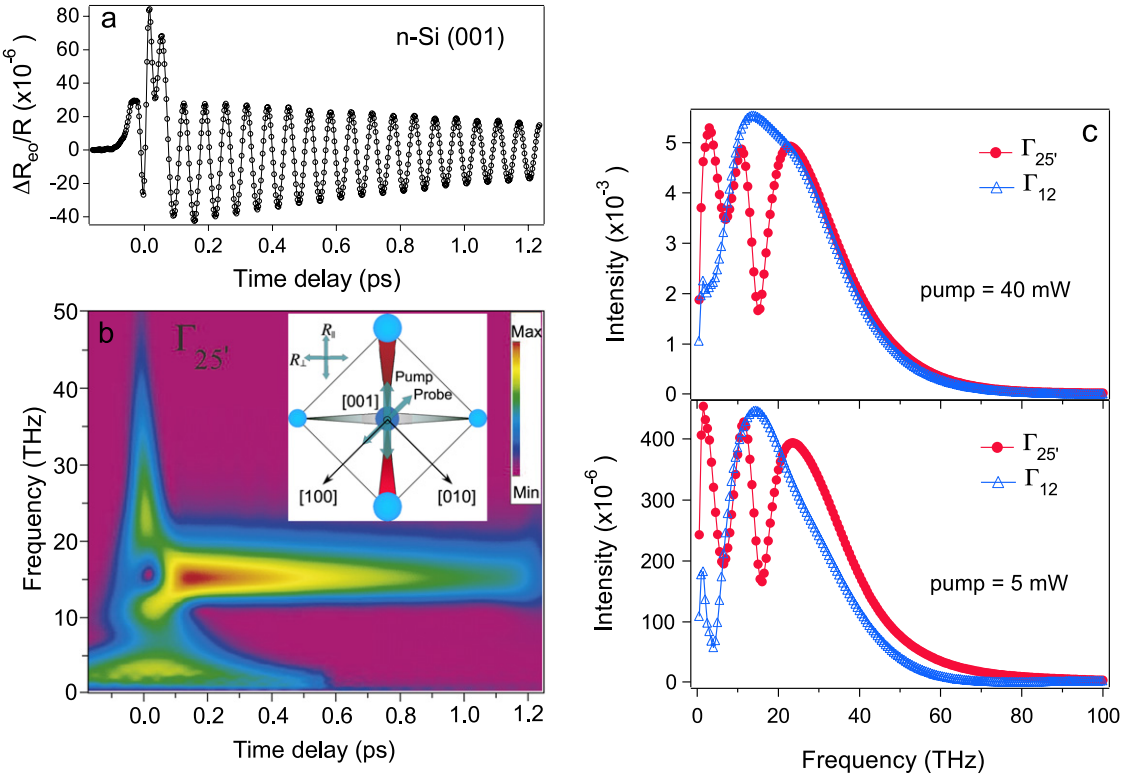

Figure 11. (a) Transient EO reflectivity change for Si(001) in $\Gamma_{25'}$ geometry. (b) Continuous wavelet transform (CWT) of (a). Insets define the polarization of the pump and probe light relative to the crystalline axes. (c) Slices of CWT spectra in (a) at zero delay for two different geometries, $\Gamma_{25'}$ and Γ_{12}. Reproduced with permission from [34]. Copyright 2003 by Nature Publishing Group.

3.2.2. Si:anisotropic carrier–phonon interaction. With heavy doping of Si, the electron–phonon coupling dynamics show different features from those of non-doped or lightly doped Si. Very recently Kato *et al* have performed time-resolved anisotropic reflectivity measurements for p-type heavily doped Si in the range 3×10^{19}–1.5×10^{20} cm^{-3} by using a sub-10 fs pulse laser with an energy of 1.55 eV (800 nm wavelength) [67].

The time-dependent EO reflectivity change of Si is shown in figures 12(a) and (b). It consists of a fast and intense carrier response and an oscillatory signal. The FT spectrum of the oscillatory signal gives a peak at 15.5 THz (see figure 12(c)), which corresponds to coherent optical phonons in Si [34, 66, 68]. Since the excitation energy is below the direct bandgap (3.4 eV) [69], a non-resonant process (or excitation across the indirect bandgap of 1.12 eV) is involved in these results, which leads to the much weaker optical phonon amplitude of $\Delta R_{eo}/R \sim 1 \times 10^{-6}$ [67] than that (see figure 11(a)) under the resonant process ($\Delta R_{eo}/R \sim 30 \times 10^{-6}$) [34].

Heavy p-type doping caused a nonoscillatory decay component in the carrier response near the $t = 0$ region. Under conditions for EO detection, isotropic carrier responses are canceled out and only anisotropic contributions to the carrier response, such as from polarization grating, anisotropic state-filling and coherent optical phonons, can be detected. The carrier response in the p-type heavily doped Si is fitted well by a linear combination of polarization grating and anisotropic state-filling; see figure 12(b). For non-doped Si and lightly doped Si, there is no contribution from anisotropic state-filling; see figure 12(a). This indicates that p-type heavy doping enhances the anisotropy in the carrier distribution. In fact, in the heavily doped p-Si, the Fermi energy is lowered about 100 meV from the top of the valence band. With the lowering of the Fermi energy, inter-valence band transitions from lower valence bands to upper ones occur; see the upward arrows in figure 12(c). The non-parabolicity of the heavy-hole band appears to cause anisotropy in the hole distribution, which should result in a larger contribution from anisotropic state-filling, as observed. In contrast, such inter-valence band transitions do not occur in non-doped Si because the Fermi level is positioned at the top of the valence band. Therefore, no contribution from anisotropic state-filling is observed. It is worth noting that different initial phases of coherent phonons were observed in the p-type heavily doped Si and the non-doped Si. The p-type heavily doped Si showed cosine-like oscillations ($\varphi_0 = 20° \pm 4°$), while the non-doped Si showed an intermediate phase between cosine- and sine-like oscillations ($\varphi_0 = 52° \pm 3°$); thick lines in insets of figures 12(a) and (b). The cosine phase in p-type heavily doped Si is explained by the enhanced anisotropy of holes [67]. Even if the photon energy is above the indirect bandgap in Si, holes are generated in the valence band. Such photo-generated holes should contribute to the generation of coherent phonons, which is beyond the framework of the RSFL theory. In fact, the contribution of holes to the generation of coherent phonons has been pointed

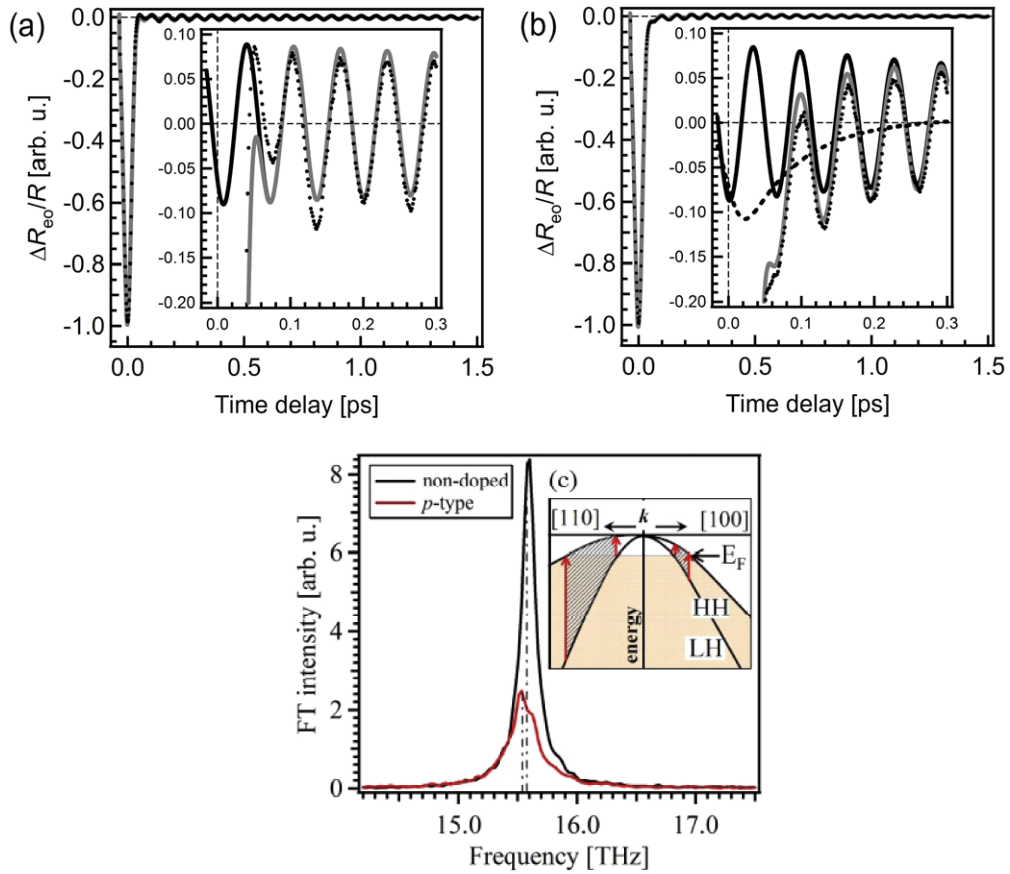

Figure 12. Fitting of the time-resolved reflectivity change for (a) non-doped Si and (b) heavily doped p-Si. Experimental data and the fitting result are shown by black dots and gray lines, respectively. Insets show enlarged graphs around $t = 0$. Black and dashed lines represent the contribution from coherent phonons and anisotropic state-filling, respectively. (c) FT spectra of the oscillatory signals in (a). Broken lines show the peak positions. The carrier response in the p-type heavily doped Si is fitted with the summed components from the polarization grating and the anisotropic state-filling (dashed line). On the other hand, in the non-doped Si and lightly doped Si, they are fitted without the anisotropic state-filling. The inset of (c) indicates the band structure of the valence band in p-Si along two directions in the Brillouin zone. HH and LH stand for the heavy-hole and the light-hole bands, respectively. Upward arrows represent the possible interband transition from LH to HH bands. The hatched area shows the region where the interband transitions are allowed. Adapted from [67].

out by Scholz *et al* [70]. In terms of carrier–phonon couplings, they showed that the anisotropy of the hole distribution is crucial for generating coherent phonon oscillations by use of an extended density-matrix model. Experimentally, it has been confirmed that p-type doping induces anisotropy in the hole distribution; see figure 12(b).

3.2.3. Metals: nonequilibrium electron–phonon dynamics. In metals, relaxation dynamics of optically excited nonequilibrium electrons has been extensively studied by TR or transient transmission (TT) pump–probe techniques using femtosecond lasers [71–75]. The electron–phonon (e–ph) thermalization occurs on a sub-picosecond timescale in metals and has been traditionally described by the use of a two temperature model (TTM) [72, 76–78]. Besides observing the dynamics of nonequilibrium electrons, pump–probe angular deflection techniques have been used to investigate coherent acoustic phonon pulses [79, 80]. The acoustic phonon pulse is generated through transient heating of the sample surface induced by excitation with intense laser pulses. The response from acoustic phonon pulses is typically observed on a several hundred picosecond timescale (or GHz frequency range) [81]. Since e–ph thermalization takes place on a sub-picosecond timescale (or THz frequency range) [72], coherent optical phonons in metals, which are impulsively excited and decay within a few picoseconds, may play an important role in the relaxation of hot electrons; see figure 13. So far, coherent optical phonons have been observed for only a few metals such as Gd and Tb [20, 82, 83], Cd and Zn [84]. In this section we discuss the e–ph interaction dynamics in Zn.

The metal sample used was a single crystal of Zn with a cut and polished (0001) surface. Femtosecond TR measurements (figure 4(b)) were carried out in a temperature range from 7 to 295 K using a cryostat. At a pump fluence of 9.2 μJ cm^{-2} (60 mW) the maximum electron temperature rise ΔT_e^m was estimated to be $\leqslant$100 K at 300 K. The sub-picosecond electronic response was extracted from the time-resolved TR measured at several temperatures, as shown in figure 14 [84]. In order to fit the time-domain data and to obtain the amplitude and relaxation time of the fast electronic transient, we utilize a linear combination of a damped harmonic oscillator and a single exponential decay

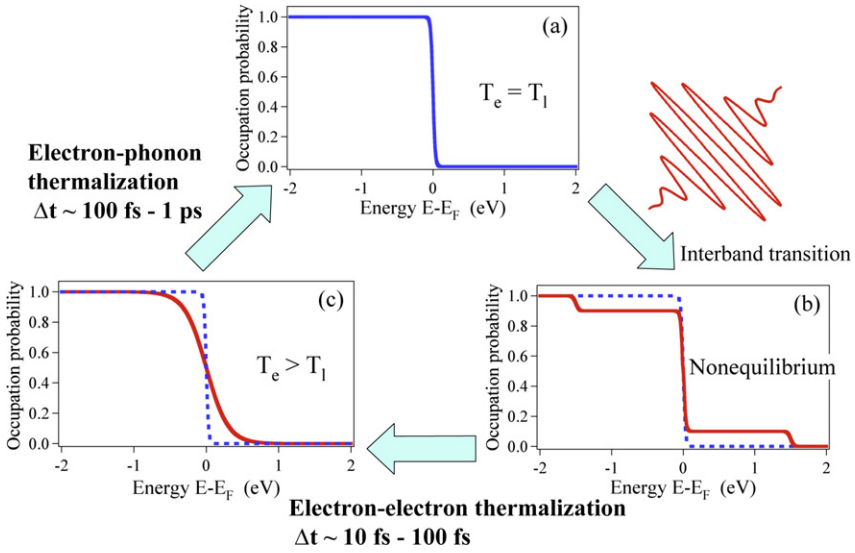

Figure 13. Dynamics of photo-generated electrons in metals. (a) Occupation probability of electrons in thermal equilibrium, where the electron temperature T_e equals the lattice temperature T_l. (b) Occupation probability of electrons in nonequilibrium just after the irradiation of femtosecond laser pulses. (c) Occupation probability of electrons after electron–electron thermalization, where $T_e > T_l$.

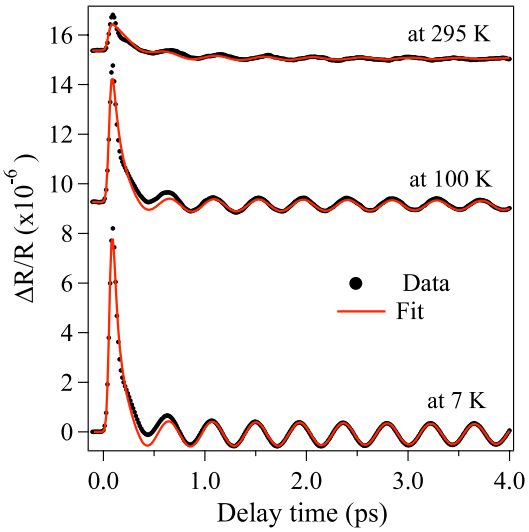

Figure 14. TR signal observed for Zn at 7, 100 and 295 K. The closed circles are experimental data, while the solid curve is the fitting with equation (6).

function:

$$\frac{\Delta R(t)}{R} = H(t)[A\mathrm{e}^{-\Gamma t}\cos(\omega_{\mathrm{E}_{2g}}t + \varphi_0) + B\mathrm{e}^{-t/\tau_q} + \text{const.}]. \tag{6}$$

Here $H(t)$ is the Heaviside function convoluted with a Gaussian to account for the finite time resolution, while B and τ_q are the amplitude and relaxation time of the fast electronic transient, respectively, and $\omega_{\mathrm{E}_{2g}}$ and Γ are the frequency and the decay rate (damping) of the coherent E_{2g} phonon, respectively. In simple metals, e.g. Au and Ag [78], the ultrafast transient is usually attributed to e–ph thermalization, which is treated by the TTM. The main idea of the TTM is that, because electron–electron (e–e) thermalization is much faster than e–ph thermalization, electrons quickly (in tens of femtoseconds) thermalize (figure 13(b) → (c)) to a temperature T_e which can be much higher than the lattice temperature T_l—resulting in Fermi level smearing (figure 13(c)). In the next stage electrons thermalize with the lattice in a characteristic e–ph thermalization time, which in metals typically is in the 100 fs–1 ps range (figure 13(c) → (a)). Since after tens of femtoseconds, when electrons have already thermalized, changes in the occupied electronic density of states are limited to energies of $k_B T_e$ near the Fermi level. Consequently, the photo-induced reflectivity dynamics tracks the time evolution of the electronic temperature, losing heat to phonons. The TTM is given by the set of two coupled heat equations [85, 86]:

$$\begin{aligned} C_e(T_e)\frac{\partial T_e}{\partial t} &= -g(T_e - T_l) + S(z,t), \\ C_l\frac{\partial T_l}{\partial t} &= g(T_e - T_l), \end{aligned} \tag{7}$$

where $C_e(T_e)$ and C_l are the respective heat capacities of electrons and lattice, g $(=g(T_l))$ is the e–ph coupling function and $S(z,t)$ describes the absorbed energy, where z is the depth coordinate. In the pump–probe experiment $S(z,t)$ is a Gaussian function. In the weak perturbation limit (when change in the electronic temperature is small compared to the initial temperature) the electronic temperature relaxation is an exponential with e–ph thermalization time, τ_{e-ph}, given by [73]

$$\tau_{e-ph} = \frac{1}{g}\frac{C_e C_l}{C_e + C_l}. \tag{8}$$

Here, in the linear response limit, $g(T_l)$ is particularly simple in the case of simple metals where the electron bandwidth is much larger than the Debye temperature Θ_D. In this case the Debye model of the e–ph coupling can be used, and therefore $g(T) = \mathrm{d}G(T)/\mathrm{d}T$, where [78, 87, 88]

$$G(T) = 4g_\infty\left(\frac{T}{\Theta_D}\right)^5 \int_0^{\Theta_D/T} \frac{x^4\,\mathrm{d}x}{\mathrm{e}^x - 1}. \tag{9}$$

Given that, the T dependence of τ_{e-ph}, equation (8), is completely determined by the e–ph coupling constant g, Θ_D and $C_e(T)$. Since the lattice specific heat C_l is a factor of 10^2 larger than the electronic specific heat ($C_l \gg C_e$) in a wide temperature range [78], and since $C_e = \gamma T_e \sim \gamma T_l$, where γ is the Sommerfeld constant, the e–ph thermalization time τ_{e-ph} reduces to

$$\tau_{e-ph} \approx \frac{C_e}{g(T_l)} = \frac{\gamma T_l}{g(T_l)}, \tag{10}$$

For $T_l \ll \Theta_D$, the function $g(T_l)$ varies as T_l^4. On the other hand, for $T_l \geqslant \Theta_D$, the function $g(T_l)$ becomes constant (g_∞) [78]. Since $\Theta_D = 234$ K for Zn metal, TTM predicts $\tau_{e-ph} \sim T_l^{-3}$ at $T_l \leqslant \Theta_D/5$ and $\tau_{e-ph} \sim T_l$ at $T_l \geqslant \Theta_D/5$ [88].

The relaxation time (τ_q) of the sub-picosecond transient in Zn obtained by fitting the data with equation (6) is shown in figure 15 as a function of lattice temperature. The relaxation time monotonically increases from 75 ± 30 to 260 ± 30 fs as the temperature increases, which is similar to the behavior observed for noble metals using TR measurements [78]. The behavior follows the prediction of the TTM at temperatures above 50 K, while no upturn in relaxation time is observed at lower temperatures. The absence of an upturn in relaxation time at low temperatures is common in metals [78], and is attributed to the fact that the basic assumption of the TTM, namely that the e–e thermalization time is fast compared to the e–ph thermalization time, fails at low temperatures. Therefore a nonthermal electron model (NEM) needs to be introduced to account for the low temperature saturation of relaxation time [78, 87, 88]. By fitting the temperature dependence of the relaxation time with equation (10) the value of the e–ph coupling constant is estimated to be $g_\infty = 6.4 \times 10^{16}$ W m^{-3} K^{-1}, which is the same order of magnitude as obtained in other simple metals [72].

We note that damping of coherent optical phonons observed in heavy rare earth elements (Gd, Tb) has been shown to be dominated by phonon–magnon scattering, which originates from spin–orbit coupling of phonon–electron and phonon–phonon scattering below the Curie temperature [82, 83]. This result indicates that additional processes, such as phonon–magnon scattering, can contribute to the scattering mechanism in specific materials. It is interesting to also note that phonon–electron coupling has enabled researchers to monitor coherent excitation of phonons (the CDW amplitude mode), which modulate the binding energy of electrons observed in angle-resolved photoelectron spectroscopy (ARPES) [89]. A similar surface-sensitive technique has been applied to explore coherent phonon modes of sp-metals on Si, generated through strong phonon–electron coupling [90, 91].

3.2.4. Temperature dependence of electronic transient. The amplitude of the fast electronic response, B in equation (6), also displays a pronounced temperature dependence, as shown in figure 16(a). The same temperature dependence is also observed for the amplitude of the oscillatory transient due to photoexcited coherent E_{2g} phonons, suggesting that the amplitudes of the fast electronic and the coherent phonon responses have the same origin.

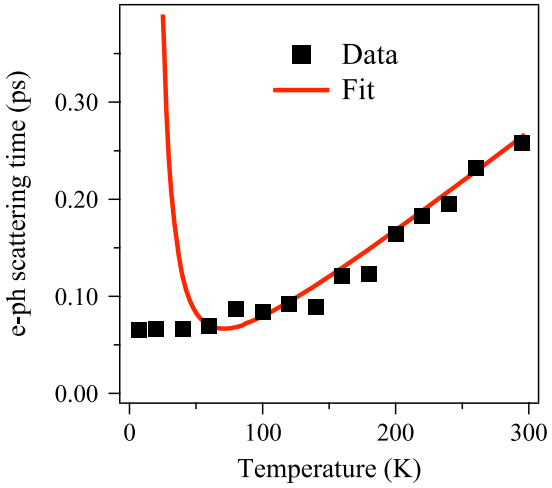

Figure 15. The temperature dependence of the electron–phonon thermalization time (τ_q). The closed squares are experimental data while the solid curve is a fit to the data with the TTM model, described by equation (10).

We derive below a formula for the temperature dependence of the transient amplitude B, which gives extremely good agreement with the data. To account for the temperature dependence, Hase *et al* made the following two assumptions: (i) the relaxation processes after excitation with short laser pulses follow the TTM, i.e., e–e thermalization is much faster than e–ph thermalization, and (ii) the changes in the reflectivity at the photon energy of 1.55 eV are due to photo-induced absorption, with photoexcited quasiparticles as initial states and with final unoccupied states well above (or below) the Fermi energy E_F [92, 93]. The latter assumption is similar to the case of optical pump–probe spectroscopy in superconductors [94] and charge density waves [14, 15]. From these assumptions, and using the Fermi golden rule, the amplitude of the transient is proportional to the change in the occupied electronic density of states near E_F, i.e. to the photo-induced quasiparticle density, n_p. In the limit when the temperature is much lower than E_F, the number density of the electron–hole pairs n is in the Landau Fermi liquid exactly proportional to temperature, $n \propto T$. Assuming that, after photoexcitation, all the absorbed energy initially goes to the electronic subsystem, one obtains

$$B \propto n_p = n_{T_e'} - n_{T_e} \propto T_e' - T_e, \tag{11}$$

where n_{T_e} is the quasiparticle density at the initial temperature T_e, while $n_{T_e'}$ is that after electrons have thermalized to the final temperature T_e'. Taking into account that the electronic specific heat $C_e = \gamma T_e$, and using the energy conservation law it follows

$$B \propto T_e' - T_e = \sqrt{T_e^2 + 2U_l/\gamma} - T_e, \tag{12}$$

where U_l is the photoexcitation energy intensity.

As shown in figure 16(a) the model (solid line) well reproduces the observed temperature dependence of the amplitude B at temperatures higher than ∼60 K. Here U_l/γ was taken as a fitting parameter. At temperatures below 50 K,

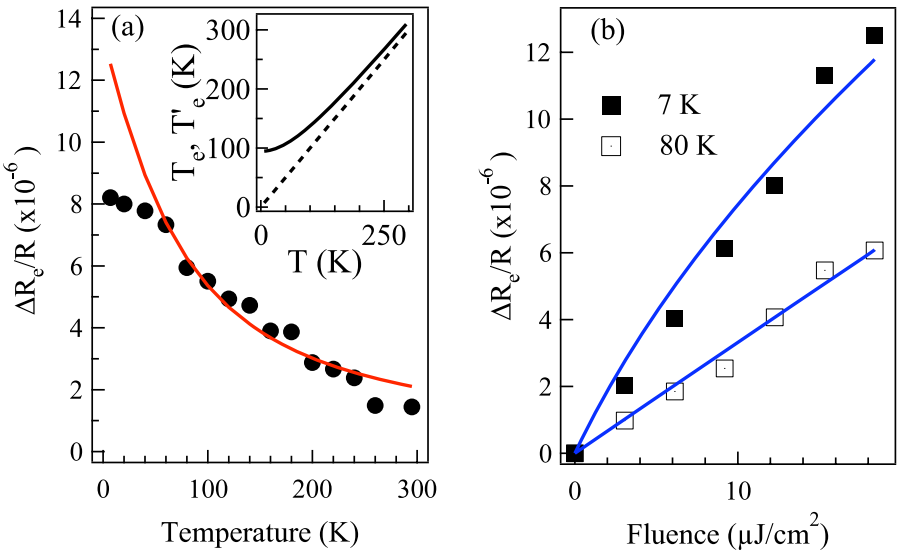

Figure 16. (a) The amplitude of the fast electronic transient as a function of temperature. Inset shows the corresponding initial (T_e—dashed) and final (T'_e—solid) electronic temperatures as a function of temperature. (b) The amplitude of the fast electronic transient versus the pump fluences at the two typical temperatures. The solid curves are the fit to the data using equation (12).

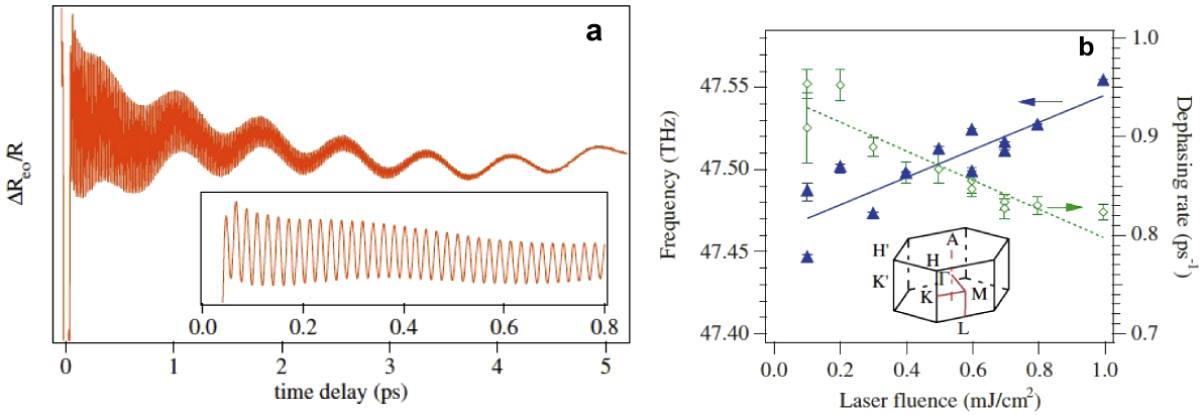

Figure 17. (a) Transient EO reflectivity change at a pump power of 50 mW. The inset shows an enlargement of the trace to show the high frequency modulation. (b) Laser fluence dependence of the dephasing rate and the frequency of the coherent E_{2g2} phonon obtained from a fit to an exponentially damped oscillator function. The lines are to guide the eyes. The inset shows the Brillouin zone of graphite. Reproduced with permission from [27]. Copyright 2008 by the American Physical Society.

on the other hand, B shows saturation, while the model predicts further increase in the amplitude. This discrepancy is ascribed to the fact that at low temperatures the TTM cannot describe the observed dynamics well, since the e–e thermalization time becomes comparable to the e–ph thermalization time [87, 88].

Figure 16(b) presents the excitation intensity dependence of the electronic amplitudes. As seen by the solid lines in figure 16(b), the model (equation (12)) predicts a sublinear dependence at 7 K, which is not observed in this intensity range, while good agreement with 80 K data is obtained. For the same reasons, the temperature dependences of relaxation time and amplitude at low temperatures do not follow the TTM prediction. The fact that electrons are nonthermal on this timescale can give rise to the absence of the sublinear intensity dependence at low temperatures.

3.2.5. Phonon–carrier couplings in graphite and carbon nanotubes. Graphite possesses a highly anisotropic crystal structure, with strong covalent bonding of atoms and weak van der Waals bonding between the hexagonal symmetry graphene sheets. Its strong e–ph interaction is a distinctive characteristic of ineffective screening of the Coulomb interactions [95], which appears as phonon frequency shifts with carrier doping [96] and strong electronic renormalization of the phonon bands (Kohn anomaly) [97].

Upon photoexcitation, coherent phonon frequency downshifts are observed in conventional materials, such as Ti_2O_3 [10], Te [5], Bi [13], and Zn [65] under intense laser excitation. The downshift is attributed to the electronic softening of the phonons by the excited carriers [5, 98–100] and/or phonon anharmonicity [13, 101, 102]. The coherent E_{2g2} of graphite is exceptional in this sense, as shown below [27]. Figure 17(a) shows the EO reflectivity change of graphite. After a fast and intense electronic response near the time-zero region, the reflectivity is modulated at two disparate periods of 21 and 770 fs. The slower coherent oscillation was assigned to the

Raman-active interlayer shear phonon (E_{2g1} mode) [39, 61]. The faster oscillation of 47.4 THz (1580 cm^{-1}) is the in-plane C–C stretching mode (E_{2g2} mode) [96] corresponding to the G-peak in the Raman spectra. The amplitude of the coherent E_{2g1} mode increases linearly with the fluence as expected for a π–π^* transition with a single photon. As shown in figure 17(b), the dephasing rate decreases as the laser fluence is increased, which is contrary to the coherent phonon response observed in other materials [13, 65, 103]. In addition, the frequency upshift at higher fluence in figure 17(b) is also contrary to that observed in other materials.

A time-windowed FT analysis of the TR response revealed that the phonon frequency upshift occurs promptly and recovers to its near-equilibrium value after several picoseconds [27]. With increasing laser fluence the initial blueshift increases, while the asymptotic value converges on the 47.4 THz Raman frequency. The experimental phonon frequency for $t > 100$ fs followed a biexponential recovery, with time constants of 210 fs and 2.1 ps, independent of excitation density. The timescales for the recovery are in reasonable agreement with the analysis of transient terahertz spectroscopy, which gave 400 fs and 4 ps, respectively, for carrier thermalization and carrier–lattice equilibration [104]. The time evolution of the E_{2g2} frequency indicates that coherent phonons interact with photoexcited nonequilibrium carriers.

The observed anomalous dispersion of the high energy phonon branches of graphite could be explained theoretically by a momentum-dependent e–ph interaction (a Kohn anomaly), which leads to the renormalization (softening) of the phonon frequency [97]. DFT calculations for a single sheet of photoexcited graphite [27] showed that the observed unusual electronic stiffening of the phonon can be attributed to the excitation-induced reduction of the e–ph coupling due to graphite's quasi-2D electronic structure (e–ph decoupling). The reduced real and imaginary parts of the complex self-energy of the e–ph interaction increase the frequency and reduces the dephasing rate of the E_{2g2} mode.

It is only recently that experimental studies for the coherent phonons for CNT have started [23, 24, 26]. In a view, the occurrence of an antenna effect may be observational evidence of e–ph coupling. Before considering the antenna effect of coherent phonons, observations of coherent optical phonons in CNTs are described. Figure 18(a) shows experimental TR measurements of the time-resolved reflectivity of bundled single-walled carbon nanotubes (SWCNTs) [26]. The transient photo-induced reflectivity consists of two components. The first component is the nonoscillatory response due to the excitation and the subsequent relaxation of excited carriers, while the second one is the oscillatory signal due to the coherent lattice vibrations. As shown in figure 18(b), the FT spectrum of the time-domain data indicates that the coherent phonon response can be separated into three frequency regions: (i) low frequency (<10 THz), (ii) 1350 cm^{-1} (40 THz) and (iii) 1560–1580 cm^{-1} (47 THz). The highest frequency component could be detected by EO reflectivity measurements [26], but the other two could not. The multiple peaks in the low frequency region correspond

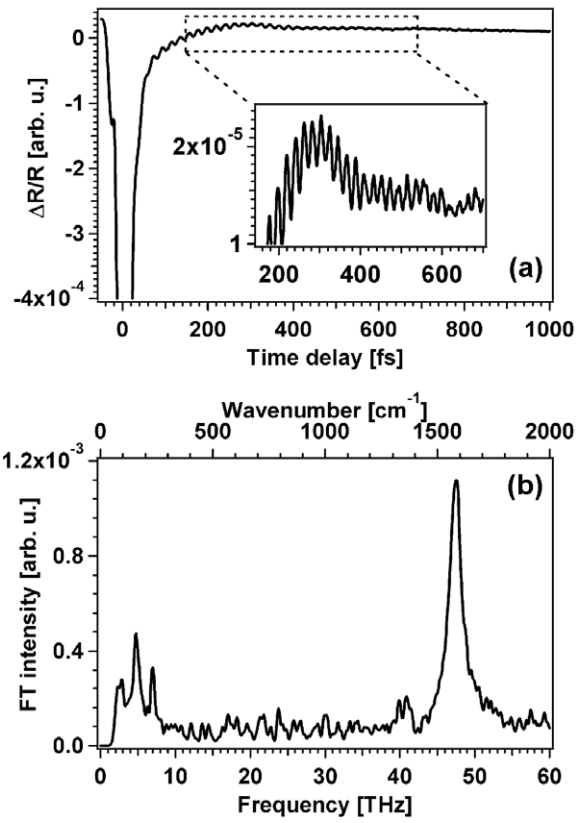

Figure 18. (a) Time-resolved transient reflectivity of SWCNTs. The inset represents the enlargement panel to show the coherent phonon oscillation. (b) FT spectrum of the time-domain datum in (a). Reproduced with permission from [26]. Copyright 2008 by the American Chemical Society.

to the radial breathing modes (RBMs) of different diameter SWCNTs; see figure 18(b) [105]. Based on Raman spectra of SWCNTs, the small peak observed at 40 THz is assigned to the disorder-induced D mode [36, 105].

The strongest peak in the FT spectra at 47 THz is the in-plane C–C stretching mode (G-peak) [105]. In the case of the G-band, the curvature of a cylindrical CNT splits the degenerate E_{2g} symmetry G-band of graphite into the higher (G^+) and lower (G^-) frequency modes [106]. For each G^+ or G^- band, the periodic boundary condition in the CNT circumferential direction defines the angular momentum of vibrational motion along the nanotube axis of 0, 1 and 2, corresponding to the A, E_1 and E_2 symmetry Raman active phonon modes [105]. Thus one expects six different G-band phonon modes in resonant Raman spectra, which can in principle be observed by polarized Raman spectroscopy [105]. The G mode should have a contribution from both the A and E symmetry modes in the TR measurements. In the bundled sample, not only the interaction between tubes but also the excitation of an electron into higher energy states lead to the short dephasing time of phonons. This should cause spectral broadening, restricting the frequency resolution and making it difficult to observe different frequencies of A, E_1, and E_2 symmetry in the G-band separately; see figure 18(b).

Phonon amplitudes of all the above-mentioned modes depend on the laser polarization with respect to the CNT axis,

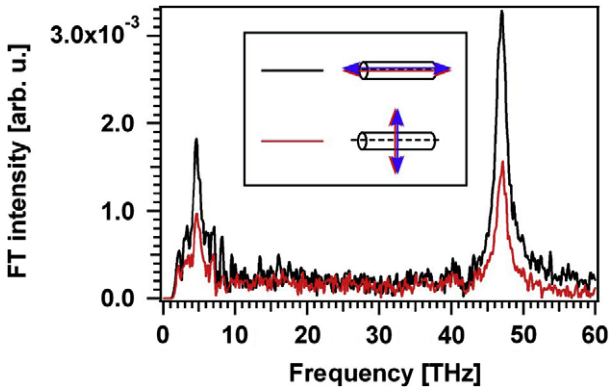

Figure 19. FT spectrum of the time-resolved reflectivity of SWCNTs with different polarization set-ups, as shown in the inset. Reproduced with permission from [26]. Copyright 2008 by the American Chemical Society.

which is expected from the antenna effect. When both the pump and probe polarization are parallel to the long axis of SWCNTs, both the RBM and G modes have higher intensity than when they are perpendicular, as shown in figure 19. This is consistent with the optical antenna effect observed in resonant Raman spectra, where optical absorption occurs preferentially for parallel polarization of the excitation light to the CNT axis [107]. Thus, figure 19 suggests that the antenna effect also dominates in the generation of coherent phonons, through an interaction with the excited carriers occurring along the axis [24].

3.3. Phonon–phonon scattering in metals, semimetals and carbon nanotubes

3.3.1. Phonon–phonon coupling in semimetals—higher harmonics. Figure 20(a) shows TR data for a single crystal of bismuth, which exhibit large amplitude coherent oscillations (A_{1g} mode) generated by a high fluence laser pulse from a regenerative 100 kHz amplifier (130 fs) [33]. The photoexcited carrier density at the maximum pump fluence of 15 mJ cm^{-2} was $\approx 6 \times 10^{21}$ cm^{-3}, which comprised 4% of all the valence electrons.

The signal consisted of nonoscillatory and oscillatory parts. For low fluences, the chirp of the phonon frequency was almost zero, while at the higher fluence, a large positive chirp was observed [13, 33]. The latter can be attributed to phonon anharmonicity. The explanation of the alternating chirp may be supported by the emergence of multi-phonon states as shown in figure 20(b), which presents the FT power spectrum of the whole timescan. This spectrum includes frequencies around ω_0, $2\omega_0$, and other higher harmonics. The observation of $2\omega_0$ is indicative of the occurrence of higher harmonics produced by phonon–phonon coupling.

3.3.2. Dephasing by anharmonic phonon–phonon coupling. Anharmonic phonon–phonon interactions are evident from the temperature dependence of the coherent phonon amplitude decay rate. Figure 21 shows the decay rate of the coherent optical phonon in single-crystal zinc as a function of the lattice temperature, measured at a pump fluence of 9.2 μJ cm^{-2}. The decay rate increases with increasing temperature. This behavior is well explained by an anharmonic decay model [44], in which the optical phonon decays into two acoustic phonons with half the frequency of the optical mode and with opposite wavevectors [43, 44]:

$$\Gamma = \Gamma_0 \left[1 + \frac{2}{\exp(\frac{\hbar\Omega_0/2}{k_B T}) - 1} \right]. \qquad (13)$$

Here Γ_0 is the effective anharmonicity used as a fitting parameter and k_B is the Boltzmann constant. Γ_0 is determined to be 0.06 ps^{-1}. The good agreement of the time-domain data with the anharmonic decay model indicates that the damping of the coherent E_{2g} mode in Zn is due to anharmonic phonon–phonon coupling. The frequency of the E_{2g} mode decreases as the temperature increases as shown in the inset of figure 21. This temperature dependence is qualitatively in good agreement with the anharmonic frequency shift observed by Raman scattering measurements [108]. A frequency shift due to lattice anharmonicity was also observed in III–V semiconductors and was reproduced by *ab initio* calculations including various anharmonic contributions (thermal expansion, third-order, and fourth-order anharmonicity) [109].

3.3.3. Superposition of different symmetry modes in carbon nanotubes. Quasi-one-dimensional CNTs, rolled-up graphene sheets, have attracted much attention due to their unique electronic and structural properties [105, 110]. One

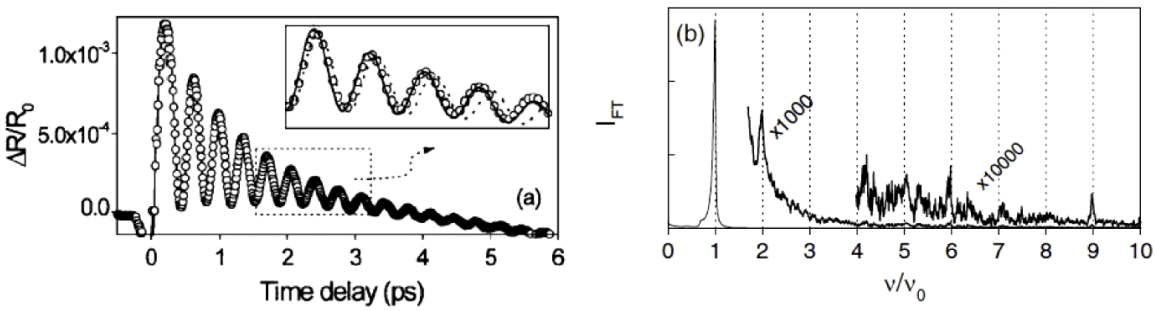

Figure 20. (a) Transient reflectivity of bismuth single crystal taken with $F = 4.8$ mJ cm^{-2} at room temperature: open symbols. The inset shows the enlarged part for the selected delays. (b) The FT spectrum for the coherent oscillations, taken with fluence $F = 14.6$ mJ cm^{-2}.

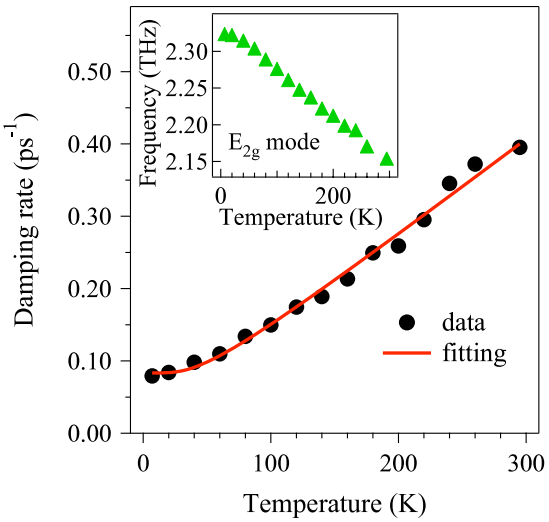

Figure 21. Decay rate of the E_{2g} mode together with the frequency (inset) as a function of the lattice temperature. The solid line represents the fit to the data using equation (13) with $\Gamma_0 = 0.06$ ps^{-1}.

important optical property of CNTs is a very fast response of the photoexcited carriers. The carrier scattering processes such as e–e, e–ph or carrier–impurity, which are important for the transport properties of CNTs, have been widely investigated by conventional optical methods. The scattering properties of high energy photoexcited carriers are determined by the emission of optical phonons on timescales less than 100 fs through strong electron–phonon or exciton–phonon interactions.

So far, there have been several reports about coherent phonons in SWCNTs as mentioned above [23, 24, 26]. By resonant excitation of specific SWCNTs with a tunable laser source having a 50 fs pulse, Lim *et al* observed the coherent RBM in SWCNT bundle samples [24]. Gambetta *et al*, who employed resonant sub-10 fs visible laser excitation, observed both the RBM and G-band mode oscillations [23]. They interpreted the anharmonic coupling between the RBM and the G-band modes as a synchronous modulation of the G mode frequency with the slower RBM oscillation. Kato *et al* [26] found an interference effect between the G-band phonons of different symmetries, using laser pulses shorter than the period of the C–C stretching mode (21 fs) for aligned SWCNTs. They made TR measurements of the SWCNTs as a function of the angle θ_1 of the pump–laser polarization with respect to the axis of the SWCNTs. The angle θ_1 is rotated, while the polarization of the probe laser was set to be perpendicular to the SWCNT axis. The G mode component had almost zero amplitude at $\theta_1 = -30°$ and 30 ° while RBMs appeared at all angles. As shown in the corresponding FT spectra, figure 22(a), the amplitude of the G mode is modulated from maxima at $\theta_1 = -90°$ and 90° to minima at $\theta_1 = -30°$ and 30°. Figure 22(b) shows the ratio between the integrated intensities of the G mode and RBM, $I(\theta_1 - \theta_2)$, as a function of $\theta_1 - \theta_2$, where θ_2 is the polarization angle of probe laser with respect to the SWCNT axis. The intensity, $I(\theta_1 - \theta_2)$, has the largest value at $\theta_1 - \theta_2 = 0°$ and 180°, while it falls almost to zero at 60° and 120°, and has a local maximum at $\theta_1 - \theta_2 = 90°$.

In order to explain the observed G mode polarization dependence, they considered the superposition of G-band phonons with different symmetries as described below. Scattering efficiencies of A, E_1 and E_2 Raman symmetries can be given by $|(a + b)/2 + (b - a)/2\cos(2\theta)|^2$, $|c \cdot \cos(2\theta)|^2$ [111, 112] and $|d(1 - \cos(2\theta))/2|^2$, respectively, where a, b, c and d are the elements of the Raman tensors [113], and θ is the pump polarization angle. The polarization dependence of the E_{2g2} symmetry phonon in graphite is well reproduced by $|\cos(2\theta)|^2$ [27]. A polarized Raman measurement [114] in CNTs experimentally shows that the G mode with A symmetry has $a = 0$ [114]. Then, the scattering efficiency of the A symmetry phonon becomes $|b/2(1 + \cos(2\theta))|^2$.

Neither the A nor the E symmetry Raman tensors alone can explain the present polarization dependence of CNTs with minima at $\theta = 60°$ and 120°. When all of the contributions from the A, E_1 and E_2 symmetries are taken into account, the total scattering intensity is given by

$$\frac{dS}{d\Omega} \propto |\alpha + \beta\cos(2\theta)|^2, \tag{14}$$

where α and β combine the elements of the Raman tensors [113]. Indeed, the observed polarization dependence in CNTs can be well reproduced by equation (14), providing $\alpha/\beta = 0.5$ (solid line in figure 22(b)). Thus, the G mode polarization dependence can be explained by the superposition of A, E_1 and E_2 symmetry Raman tensors. From the fact that frequencies of G-band phonon modes with A and E symmetries are close to each other, the disappearance of the total G-band phonon amplitude at a certain angle in our time-domain data suggests that the G-band phonons with different symmetries may oscillate with different phases [26].

4. Applications of phonon coupling

4.1. Phase transitions in ferroelectrics and optical recording media

Understanding structural phase transitions in ferroelectric materials is an extremely important issue because of their wide application in modern rewritable memory media and other electro-optic devices [88], as well as a fundamental interest in lattice dynamics [115].

One attractive application of ferroelectric materials is the controllability of spontaneous polarization using an external electric field, which makes it possible to induce soft mode hardening [116], and to study domain wall dynamics [117]. Furthermore, intense femtosecond laser pulses may also be capable of controlling ferroelectric-domain orientation [118]. In the past decade, a number of scientists have attempted to achieve optical control of the domain orientation in ferroelectric materials by using multiple pulse excitation techniques with precision timing to suppress or enhance the amplitudes of coherently excited soft modes [119]. However, this optical method has not yet succeeded in being able to control the domain orientation.

Structural phase transitions in ferroelectric materials have been investigated extensively by monitoring the soft mode, i.e.

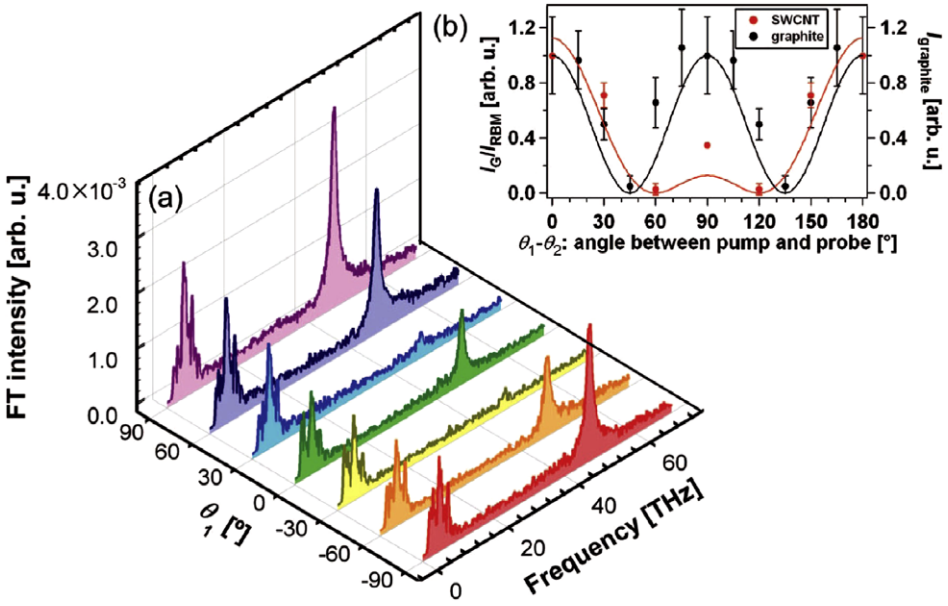

Figure 22. (a) FT spectra obtained from time-domain $\Delta R/R$ signal as the functions of the frequency and the polarization angle θ_1. (b) The ratio of the intensity of the coherent phonon spectra of the G-mode to the RBM as a function of the angle between the pump and probe beams. Reproduced with permission from [26]. Copyright 2008 by the American Chemical Society.

the lowest frequency transverse optical (TO) phonon, whose zone center frequency, ω_{TO}, is connected to the static dielectric constant, ϵ_0, by the Lyddane–Sachs–Teller relation and is drastically reduced toward zero frequency near the critical point T_c [115]. By using frequency-domain techniques, such as Raman and neutron scattering, the temperature dependence of ω_{TO} has been studied [115]. In terms of the anharmonic lattice potential [120], the phase transition in perovskites is characterized by a double-well potential with each well corresponding to a different domain orientation [120]. This is referred to as a fluctuation-driven order–disorder model; see figure 23(a). The ionic motion associated with the soft mode in displacive type ferroelectrics is, on the other hand, characterized by a single-well potential whose minimum position shifts at T_c; see figure 23(b).

Coherent phonon spectroscopy is a powerful tool for studying the ultrafast dynamics of structural phase transitions, which occur at pico- and femtosecond timescales, and has been applied both to ferroelectric materials [121–124] and Mott insulators [125, 126].

4.1.1. Structural phase transitions in GeTe. Ferroelectric GeTe has first been examined as a model sample because of the considerable interest in its application for optical memories using its reversible structural change [127]. The crystal undergoes the rhombohedral–rocksalt structural change at the transition temperature $T_c = 657 \pm 100$ K, which is attributed to a displacive phase transition [128]. In a displacive phase transition, conversion between the two phases generally involves lattice vibrations (soft mode) [129]. As mentioned above, this type of phase transition is characterized by a single potential minimum whose position shifts at T_c, while the other type of phase transition, order–disorder transition, is characterized by several potential minima among which a choice is made at T_c [129]. The order–disorder transition occurs with collective tunneling or thermally assisted hopping modes. For GeTe, the A_{1g} mode has been considered to be the soft mode, and it has been observed by Raman measurements [128]. An *ab initio* theoretical investigation predicts that the phase transition in GeTe is a fluctuation-driven first-order transition [130]. Because of the strongly reduced frequency of the soft mode near T_c, monitoring the dynamics of the phase transition is difficult with conventional frequency-domain spectroscopies [131]. To overcome these difficulties, Nelson and co-workers conducted time-resolved pump–probe measurements at various lattice temperatures in perovskites, and observed heavily damped soft phonons near T_c [121]. In this section, a study in which the critical point was approached by increasing the phonon amplitude instead of changing the lattice temperature will be described. This approach is motivated by the idea that nonthermal phase transitions can be produced by photoexcitation of the electron–phonon system; see figure 24. The sample studied was a single crystal of GeTe prepared by a vapor growth method and cleaved in the c-crystallographic plane. GeTe is a narrow bandgap semiconductor, where the generation of coherent A_{1g} phonons follows the excitation of carriers from the valence band to higher energy bands, i.e., DECPs [9]. The pump fluence was reduced by a neutral density filter to below 13 mJ cm^{-2} to prevent damaging the sample or causing laser ablation, and was varied from 0.8 to 12.7 mJ cm^{-2}. The probe fluence was also reduced and fixed at 0.3 mJ cm^{-2}.

By adding two mirror arms to a Michelson interferometer [12], a THz-rate pulse train with four pulse sequence can be generated with a variable repetition rate as shown in figure 25(b). Moving the mirror arms in the twin interferometer controls the separation time $\Delta t_{i,j}$ $(i, j = 1, 2, 3, 4)$ between the pulse components P_i and P_j. Time derivatives of the transient reflectivity changes obtained using multiple pump pulses

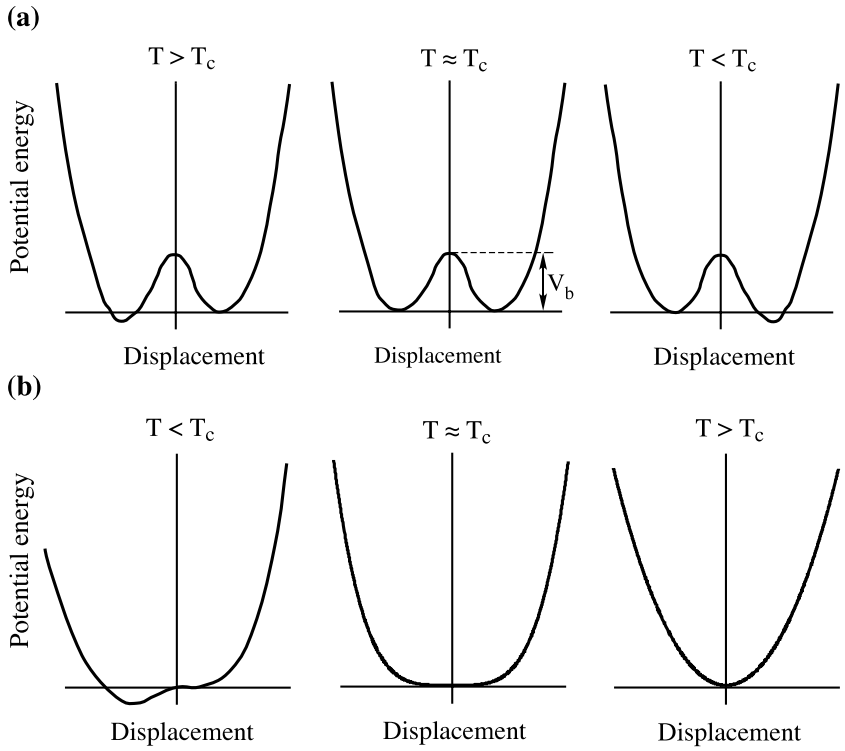

Figure 23. Local (single unit cell) potential energy diagrams for order–disorder (a) and displacive phase transitions (b). The order–disorder transition diagram indicates a double-well potential surface with a barrier height $V_b \gg k_B T_c$, where k_B is Boltzmann's constant. The displacive transition diagram indicates a single-well potential whose minimum is 'displaced' at temperatures below $T = T_c$.

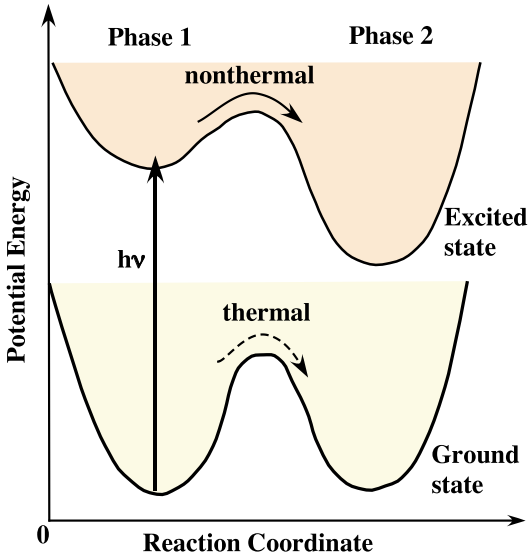

Figure 24. An illustration of the mechanism for the laser-induced nonthermal phase transition. The dashed arrow indicates phase change (from phase 1 to 2) occurring for thermodynamical equilibrium, while the solid arrow indicates phase change (from phase 1 to 2) occurring for nonthermal process.

are shown in figure 25(a). Here, the fluence of each pump pulse is 3.8 mJ cm^{-2}, so that the maximum total pump fluence (3.8 mJ cm^{-2} × 4) exceeds that of the single pump excitation (12.7 mJ cm^{-2}) without sample damage. Our intent was to have each pump pulse forces oscillation of the coherent A_{1g} mode through repetitive excitation. In order to sufficiently drive soft phonons into in-phase motion, the time intervals in the THz-rate pulse train were set to be unequal; as shown at the top of figure 25(a). The pulse delay, $\Delta t_{i,j}$, was increased for each subsequent pulse to match the longer pulse interval of each driven phonon oscillation. The time-domain data in figure 25(a) clearly demonstrate the enhancement of the amplitude of the coherent A_{1g} mode by repetitive excitation. Moreover, a drastic decrease in the dephasing time of the coherent phonons is observed. In figure 25(a), by fitting the data, we obtained the dephasing time of the coherent phonons and the frequency of the A_{1g} mode for various total pump fluences.

Figure 25(c) shows the frequency of the A_{1g} mode obtained from the fitted data as a function of the total pump fluence together with the results of single pump excitation. The A_{1g} frequency decreases linearly from 3.8 to 2.5 THz as the number of pulses in the sequence increases, while those obtained with single pulse excitation saturates at higher fluence. The dephasing time decreases from 570 to 180 fs as the number of pulses increases. The largest damping rate, $\gamma \sim 1.8$ ps^{-1} ($=1/(180\text{ fs})/\pi$), which was observed with four pump pulses, is close to the frequency of $\omega \sim 2.5$ ps^{-1} (or 2.5 THz), indicating that the A_{1g} mode was driven close to the critical damping point ($\omega = \gamma$).

We note that the lowest frequency of the soft mode observed in the present study using a THz-rate pulse train (2.5 THz) is comparable to the incoherent phonon frequency at a temperature of ≈590 K according to the Curie–Weiss law [128], verifying that the crystal lattice is quite close to the transition point.

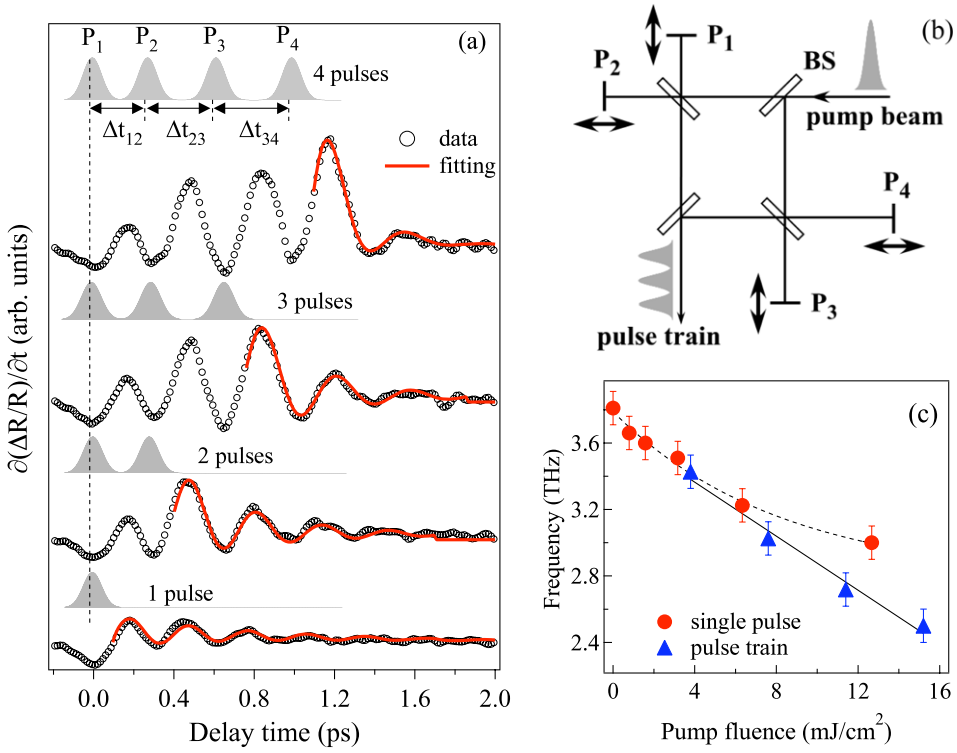

Figure 25. (a) Repetitive excitation of the A_{1g} mode using THz-rate pulse train. P_1, P_2, P_3, P_4 are the first, second, third, fourth pump pulses, respectively. Δt_{12}, Δt_{23} and Δt_{34} are set to be 290 fs, 320 fs and 345 fs, respectively. The open circles represent the experimental data. The solid lines represent the fitting of the time-domain data after the final pumping pulse using a damped harmonic oscillation. (b) The optical layout of a twin Michelson interferometer for the generation of the pulse train. BSs are the beam splitters. Each mirror arm labeled P_i ($i = 1, 2, 3, 4$) is computer controlled. (c) The pump fluence dependence of the frequency of the A_{1g} mode obtained for the single pump pulse and the pulse train, respectively. The dotted curve is an eye guide and the solid line corresponds to a fitting of the data with a linear function.

The multiple pump excitation technique provides a new pathway for manipulating collective atomic motions [132, 133]. We mention two very recent examples. Kim *et al*, have made a preferential selection of specific RBM with different chiralities in CNTs by using a pulse shaping technique [134]. Watanabe *et al* have attempted to control surface chemical reactions by means of the similar mode-selective excitation of coherent surface phonons in metals [135].

4.1.2. Phase change in optical recording media, $Ge_2Sb_2Te_5$. One of the most common materials for optical recording media, e.g. DVD discs, is $Ge_2Sb_2Te_5$ (GST), in which the transition between crystalline and amorphous phases enables rewritable recording [136, 137]. Recently, extensive theoretical investigations of the mechanism of the phase change in GST have been conducted using molecular dynamics simulations [138–140]. In addition, experimental studies using extended x-ray absorption fine structure (XAFS) and Raman scattering measurements have examined the dynamics of the phase transition in GST [141–144]. The results suggest that the structure of amorphous GST can be described as a cross section of a distorted rocksalt structure containing vacancies. The amorphization of GST is considered to be caused by an umbrella flip of Ge atoms from an octahedral position into a tetrahedral one. Moreover, in a theoretical study Sun *et al* proposed that vacancies in crystalline (cubic) GST are highly ordered and layered [139].

One of the advantages of GST as an optical recording medium is its high speed switching of read–write characteristics, whose timescale has been believed to be less than a nanosecond. Moreover, a new class of semiconductor superlattices ($GeTe/Sb_2Te_3$) with three different states has recently been proposed, which would enable reversible transitions among the three states using laser pulse irradiation [145]. Here we introduce recent developments in understanding the effects of coherent lattice dynamics on GST.

The samples used were GST films (18 nm thick) fabricated on an Si(100) substrate using a helicon wave RF magnetron sputtering machine. Annealing the as-grown GST films at 493 K (220 °C) for 10 min changed the amorphous states into the crystalline state [146]. Excitation of the GST films with 850 nm (=1.46 eV) laser pulses generated photo-carriers across a narrow band gap of ≈0.5–0.7 eV [147].

Figure 26 shows the TR signal ($\Delta R/R$) observed in GST films with amorphous (as-grown) and crystalline (annealed) phases at 295 K. After the transient electronic response due to the excitation of photo-carriers at $t = 0$, coherent phonon oscillations with a few picoseconds dephasing time appear. The corresponding FT spectra are obtained from the full scan of the time-domain data as shown in the inset of figure 26, in which two broad peaks are observed at 4.70 and 3.66 THz in the amorphous film, while the sharp peak at 3.66 THz and a broad weaker band at ≈4.9 THz are observed in the crystalline film. The peaks in the amorphous film can be considered to

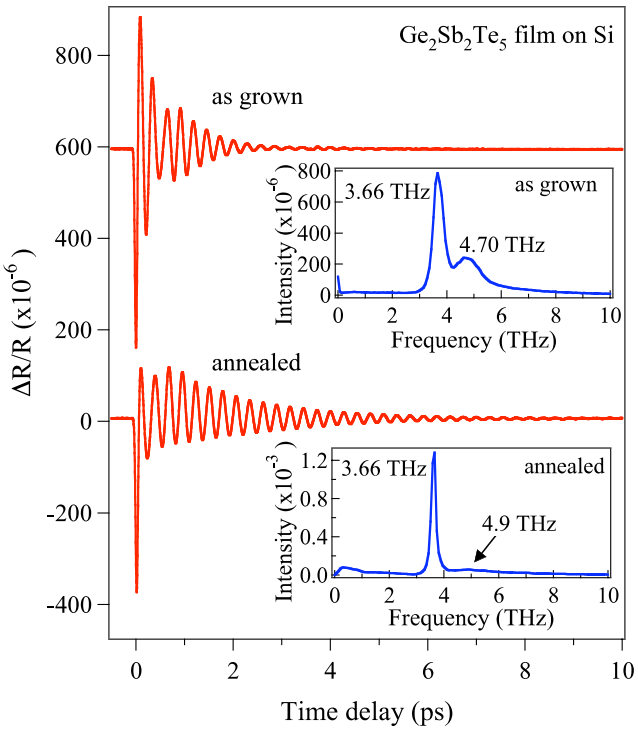

Figure 26. The TR signal observed in amorphous and crystalline $Ge_2Sb_2Te_5$ films at 295 K. The insets represent FT spectra obtained from the time-domain data.

be the A_1 optical mode due to tetrahedral $GeTe_4$ structure for the 3.66 THz peak [148], and the A_1 optical mode due to disordered Te–Te chains [148, 142] or the A_1 optical mode due to Sb_2Te_3 sublattice, as recently proposed [144], for the 4.70 THz peak. The peaks in the crystalline phase at 3.66 THz and ≈4.9 THz are in good agreement with those observed by Först *et al*, although the peak at 2.0 THz is not detected in the present study as was observed in past experiments [148]. The difference in the FT spectra found in the crystalline films could be due to the sample condition; we annealed the amorphous GST film at 220 °C, while the coherent phonons were detected at an elevated temperature of 160 °C in the past work [148], so the local structure of GST could be slightly different in each case.

Our idea that coherent control of the coherent A_1 optical mode would induce rapid conversion between the amorphous and the crystalline phases has been examined with the multiple pump pulse technique, and further investigation of this intriguing phenomenon is under way [149].

Although here we have presented phase transition dynamics studies in a limited class of materials, coherent phonon spectroscopy has been applied to other potential systems, such as charge-density-wave (CDW) materials [14, 15, 89, 150] and superconductors [17, 18]. Note that coupling between an optical phonon and the Kondo effect has recently been explored by monitoring the electronic and phononic dynamics on an ultrafast timescale [151]. In addition to conventional optical pump–probe techniques, recent advances in the generation of light pulses in the extreme wavelength regime (ultrafast x-ray, XUV attosecond and terahertz pulses) have made it possible to measure coherent vibrational motion in solids (phonons or plasmons) more directly [152, 64, 153, 154]. These innovative new probe regimes will no doubt provide a deeper understanding of the lattice and surface dynamics during structural phase transitions.

4.2. Phonon coupling as a monitor of pH environments

4.2.1. Coherent phonons in carbon nanotubes in different pH environments. In this section, we present measurements of the coherent oscillation of RBMs in SWCNTs for various pH environments and show that the sub-picosecond relaxation dynamics as well as the coherent phonon spectra of the RBM are very sensitive to changes in SWCNT electronic structure [155, 156].

Samples of SWCNTs were produced via the high-pressure catalytic CO decomposition (HiPco) process. To disperse SWCNTs in aqueous solution, sodium dodecyl sulfate (SDS) was used. A solution containing 100 mM SDS in distilled water was mixed with the SWCNT powder. The SWCNTs were dispersed by ultrasonication for 30 min at 20 °C. Non-dispersed SWCNTs were removed by filtration of the solution using Whatman filter paper no. 41. Successively, they were diluted threefold into 50 mM citrate phosphate–borate buffer solutions at different pHs (3, 4, 5, 6 and 7), and aliquots were placed into 5 mm thick quartz cells. Absorption spectra obtained for SWCNTs in SDS solution showed that sharp peaks corresponding to the exciton bands [157] appeared and that the absorbance at ≈850 nm gradually increased as the pH value increased. The transient transmission ($\Delta T/T$) was recorded as a function of the pump–probe time delay τ using 20 fs pulses at 850 nm. We find in figure 27 that the model fits the time-domain data well, although there is a significant discrepancy between the data and the fit at the early time stage, i.e. within the first oscillation cycle at ⩽300 fs. Two dominant RBMs were observed at 6.4 and 7.2 THz, and their spectral intensities depended on the pH value [158]. The enhancement of the lower RBM (6.4 THz) at the higher pH values could be attributed to the change in the electronic structure from a p-doped to a non-doped state by the deprotonation effect. Dephasing times of the lower RBM extracted from the time-domain data exhibited a pH dependence, which was explained by electron–phonon coupling through the deformation potential, while that of the higher RBM did not depend on pH, implying electron–phonon decoupling in a few picoseconds.

5. Summary and conclusions

In this paper, we have reviewed experiments to study the ultrafast coherent response of phononic environments in condensed matter. Exploiting the femtosecond real-time dynamics of coherent phonons in various materials, we have investigated coherent lattice motions, whose dephasing properties are affected by the interactions with phononic environments, such as carriers (electrons and holes), thermal phonons and point defects in crystalline solids.

In semimetals (Bi and graphite) phonon–defect scattering accelerates the dephasing of coherent phonons, where the

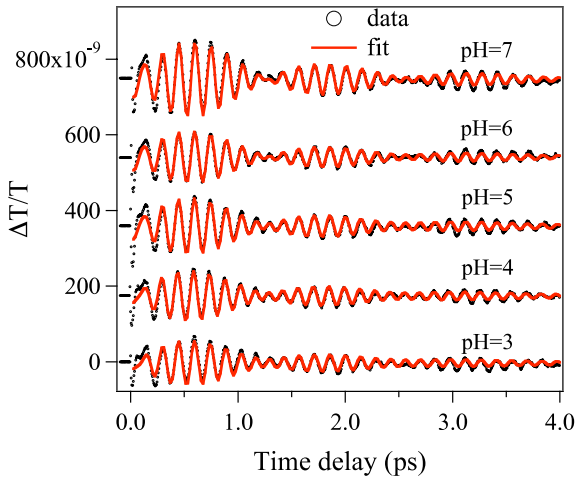

Figure 27. Time-domain signal from the coherent RBM in SWCNTs obtained by subtracting carrier responses from the transient transmission $\Delta T/T$ at various pH values. The solid lines represent the fit to the time-domain data with a linear combination of the damped harmonic oscillators.

dephasing rate linearly increases with the defect density. In semiconductors (e.g. GaAs), capture of carriers with defects dominates the annihilation of phonon–plasmon coupled modes.

Phonon–electron scattering in Si exhibited a Fano-type interference effect in time–frequency space, which showed destructive interference within 100 fs after the photoexcitation. The time-dependent EO reflectivity change of heavily doped p-type Si excited under a non-resonant condition showed a cosine-like initial phase and renormalization effects of the coherent optical phonons due to strong phonon–hole interactions. For the metal Zn, hot (nonequilibrium) electrons dominate the dynamics of both relaxation and generation of the coherent optical phonons in a wide range of the lattice temperature.

The frequency chirp of coherent phonons can be a direct measure of phonon–carrier couplings. Using sub-10 fs pulsed laser, coherent optical phonons in graphitic materials have been observed. Usually the frequencies get downshifted through electronic softening (anharmonic effect as well under high-density photoexcitation). In this sense graphite is exceptional, where the frequency is upshifted upon photoexcitation, being explained in terms of electron–phonon decoupling.

The formation of higher harmonics of the coherent phonons gives direct evidence for phonon–phonon couplings, as has been evident in semimetals. CNTs show an unexpected polarization dependence on the intensities of the coherent phonon spectra due to the existence of many modes with different symmetries, resulting in the superposition (or interference) between them.

One of the most interesting applications is the selective excitation of specific phonon modes through the pulsed train technique. We have shown only fundamental experiments on ferroelectrics to illustrate the possibility of controlling structural phase transformations. This technique can be applied also to controlling chemical reactions in solids (or their surfaces), and appears very promising because it is of wide application. It should be possible to control collective atomic motions coherently and effectively in solids if the carrier envelope phase of the light source is precisely controlled. Thus, it appears that coherent phonon spectroscopy will potentially open new avenues for research in solids.

Acknowledgments

The authors acknowledge K Ishioka, L Rong, K Kato, K Ushida, H Petek, O V Misochko, S Nakashima, K Mizoguchi, J Tominaga, S Sugai, J Demsar, A M Constantinuscu, S Hishita, R Saito and J Tang for their significant contributions to the studies presented, and R Bastasz for stimulating discussions and his helpful comments. This work was financially supported by a Grant-in-Aid for the Scientific Research from the Ministry of Education, Culture, Sports, Science and Technology of Japan under grant KAKENHI-15740188, 15035219, 18340093, 19540329 and 21310065.

References

[1] Nelson K A, Dlott D D and Fayer M D 1979 *Chem. Phys. Lett.* **64** 88
[2] Cho G C, Kütt W and Kurz H 1990 *Phys. Rev. Lett.* **65** 764
[3] Kütt W, Albrecht W and Kurz H 1992 *IEEE J. Quantum Electron.* **28** 2434
[4] Yamamoto A, Mishina T and Masumoto Y 1994 *Phys. Rev. Lett.* **73** 740
[5] Hunsche S, Wienecke K, Dekorsy T and Kurz H 1995 *Phys. Rev. Lett.* **75** 1815
[6] Baumberg J J and Williams D A 1997 *Phys. Rev. Lett.* **78** 3358
[7] Cheng T K, Bronson S D, Kazeroonian A S, Moodera J S, Dresselhaus G, Dresselhaus M S and Ippen E P 1990 *Appl. Phys. Lett.* **57** 1004
[8] Cheng T K, Vidal J, Zeiger H J, Dresselhaus G, Dresselhaus M S and Ippen E P 1991 *Appl. Phys. Lett.* **59** 1923
[9] Zeiger H J, Vidal J, Cheng T K, Ippen E P, Dresselhaus G and Dresselhaus M S 1992 *Phys. Rev.* B **45** 768
[10] Cheng T K, Acioli L H, Vidal J, Zeiger H J, Dresselhaus G, Dresselhaus M S and Ippen E P 1993 *Appl. Phys. Lett.* **62** 1901
[11] Garrett G A, Albrecht T F, Whitaker J F and Merlin R 1996 *Phys. Rev. Lett.* **77** 3661
[12] Hase M, Mizoguchi K, Harima H, Nakashima S, Tani M, Sakai K and Hangyo M 1996 *Appl. Phys. Lett.* **69** 2474
[13] Hase M, Kitajima M, Nakashima S I and Mizoguchi K 2002 *Phys. Rev. Lett.* **88** 067401
[14] Demsar J, Biljakovic K and Mihailovic D 1999 *Phys. Rev. Lett.* **83** 800
[15] Demsar J, Forró L, Berger H and Mihailovic D 2002 *Phys. Rev.* B **66** 041101(R)
[16] Toda Y, Tateishi K and Tanda S 2004 *Phys. Rev.* B **70** 033106
[17] Albrecht W, Kruse Th and Kurz H 1992 *Phys. Rev. Lett.* **69** 1451
[18] Misochko O V, Kisoda K, Sakai K and Nakashima S 2000 *Phys. Rev.* B **61** 4305
[19] Misochko O V, Georgiev N, Dekorsy T and Helm M 2002 *Phys. Rev. Lett.* **89** 067002
[20] Melnikov A, Radu I, Bovensiepen U, Krupin O, Starke K, Matthias E and Wolf M 2003 *Phys. Rev. Lett.* **91** 227403
[21] Bovensiepen U, Melnikov A, Radu I, Krupin O, Starke K, Wolf M and Matthias E 2004 *Phys. Rev.* B **69** 235417

[22] Watanabe K, Takagi N and Matsumoto Y 2004 *Phys. Rev. Lett.* **92** 057401
[23] Gambetta A, Manzoni C, Menna E, Meneghetti M, Cerullo G, Lanzani G, Tretiak S, Piryatinski A, Saxena A, Martin R L and Bishop A R 2006 *Nat. Phys.* **2** 515
[24] Lim Y-S, Yee K-J, Kim J-H, Hároz E H, Shaver J, Kono J, Doorn S K, Hauge R H and Smalley R E 2006 *Nano Lett.* **6** 2696
[25] Ishioka K, Hase M, Kitajima M and Petek H 2006 *Appl. Phys. Lett.* **89** 231916
[26] Kato K, Ishioka K, Kitajima M, Tang J, Saito R and Petek H 2008 *Nano Lett.* **8** 3102
[27] Ishioka K, Hase M, Kitajima M, Wirtz L, Rubio A, Saito R and Petek H 2008 *Phys. Rev.* B **77** 121402(R)
[28] Lüer L, Gadermaier C, Crochet J, Hertel T, Brida D and Lanzani G 2009 *Phys. Rev. Lett.* **102** 127401
[29] Yan Y-X, Gamble E B Jr and Nelson K A 1985 *J. Chem. Phys.* **83** 5391
[30] Merlin R 1997 *Solid State Commun.* **102** 207
[31] Dekorsy T, Cho G C and Kurz H 2000 *Light Scattering in Solids VIII* ed M Cardona and G Güntherodt (Berlin: Springer) chapter 4
[32] Kuznetsov A and Stanton Ch 1999 *Ultrafast Phenomena in Semiconductors* ed K-T Tsen (Berlin: Springer)
[33] Misochko O V, Hase M, Ishioka K and Kitajima M 2004 *Phys. Rev. Lett.* **92** 197401
[34] Hase M, Kitajima M, Constantinescu A M and Petek H 2003 *Nature* **426** 51
[35] Harrison W A 1970 *Solid State Theory* (*International Series in Pure and Applied Physics*) ed L I Schiff (New York: McGraw-Hill) chapter 2
[36] Kitajima M 1997 *Crit. Rev. Solid State Mater. Sci.* **22** 275
[37] Schiff L I 1968 *Quantum Mechancs* 3rd edn (New York: McGraw-Hill) (Tokyo: Kogakusha)
[38] Hase M, Ishioka K, Kitajima M, Ushida K and Hishita S 2000 *Appl. Phys. Lett.* **76** 1258
[39] Ishioka K, Hase M, Kitajima M and Ushida K 2001 *Appl. Phys. Lett.* **78** 3965
[40] Yu P Y and Cardona M 1999 *Fundamentals of Semiconductors* (Berlin: Springer)
[41] Ashcroft N W and Mermin N D 1976 *Solid State Physics* (New York: Holt, Rinehart and Winston)
[42] Ziegler J F, Biersack J P and Littmark U 1985 *The Stopping and Range of Ions in Solids* vol 1 (New York: Pergamon)
[43] Hase M, Mizoguchi K, Harima H, Nakashima S and Sakai K 1998 *Phys. Rev.* B **58** 5448
[44] Vallée F 1994 *Phys. Rev.* B **49** 2460
[45] Souza J P, Danilov I and Boudinov H 1997 *J. Appl. Phys.* **81** 650
[46] Auret F D, Meyer W E, Deenapanray P N K, Goodman S A, Myburg G, Murtagh M, Ye S-R and Crean G M 1998 *J. Appl. Phys.* **84** 1973
[47] Dharmarasu N, Sundarakkannan B, Kesavamoorthy R, Nair K G M and Kumar J 1999 *Physica* B **262** 329
[48] Shah J 1999 *Ultrafast Spectroscopy of Semiconductors and Semiconductor Nanostructures* (*Springer Series in Solid-State Sciences*) ed M Cardona, chapters 2–5
[49] Johnson M B, McGill T C and Paulter N G 1989 *Appl. Phys. Lett.* **54** 2424
[50] Gupta S, Whitaker J F and Mourou G A 1992 *IEEE J. Quantum Electron.* **28** 2464
[51] Benjamin S D, Loka H S, Othonos A and Smith P W E 1996 *Appl. Phys. Lett.* **68** 2544
[52] Dekorsy T, Kurz H, Zhou X Q and Ploog K 1993 *Appl. Phys. Lett.* **63** 2899
[53] Mooradian A and MaWhorter A L 1967 *Phys. Rev. Lett.* **19** 849
[54] Katayama S, Hase M, Iida M and Nakashima S 2001 *Proc. 25th Int. Conf. on the Physics of Semiconductors* (*Springer Proc. in Physics*) ed N Miura and T Ando (Berlin: Springer) p 180
[55] Cho G C, Dekorsy T, Bakker H J, Hövel R and Kurz H 1996 *Phys. Rev. Lett.* **77** 4062
[56] Hase M, Mizoguchi K, Harima H, Miyamaru F, Nakashima S, Fukasawa R, Tani M and Sakai K 1998 *J. Lumin.* **76/77** 68
[57] Hase M 2009 *Appl. Phys. Lett.* **94** 112111
[58] Hase M, Ishioka K, Kitajima M and Ushida K 2003 *Appl. Phys. Lett.* **82** 3668
[59] Hase M, Nakashima S, Mizoguchi K, Harima H and Sakai K 1999 *Phys. Rev.* B **60** 16526
[60] Seibert K, Cho G C, Kütt W, Kurz H, Reitze D H, Dadap J I, Ahn H, Downer M C and Malvezzi A M 1990 *Phys. Rev.* B **42** 2842
[61] Mishina T, Nitta K and Masumoto Y 2000 *Phys. Rev.* B **62** 2908
[62] Pfeifer T, Kütt W, Kurz H and Scholz R 1992 *Phys. Rev. Lett.* **69** 3248
[63] Lee J D, Inoue J and Hase M 2006 *Phys. Rev. Lett.* **97** 157405
[64] Huber R, Tauser F, Brodschelm A, Bichler M, Abstreiter G and Leitenstorfer A 2001 *Nature* **414** 286
[65] Hase M, Demsar J and Kitajima M 2006 *Phys. Rev.* B **74** 212301
[66] Riffe D M and Sabbah A J 2007 *Phys. Rev.* B **76** 085207
[67] Kato K, Ishizawa A, Oguri K, Tateno1 K, Tawara T, Gotoh H, Kitajima M and Nakano H 2009 *Japan. J. Appl. Phys.* **48** 100205
[68] Sabbah A J and Riffe D M 2002 *Phys. Rev.* B **66** 165217
[69] Adachi S 1988 *Phys. Rev.* B **38** 12966
[70] Scholz R, Pfeifer R and Kurz H 1993 *Phys. Rev.* B **47** 16229
[71] Diels J-C and Rudolph W 1996 *Ultrashort Laser Pulse Phenomena: Fundamentals, Techniques, and Applications on a Femtosecond Time Scale* (New York: Academic) chapter 8
[72] Hohlfeld J, Wellershoff S-S, Güdde J, Conrad U, Jäanke V and Mattias E 2000 *Chem. Phys.* **251** 237
[73] Sun C K, Vallée F, Acioli L H, Ippen E P and Fujimoto J G 1993 *Phys. Rev.* B **48** R12365
[74] Fann W S, Storz R, Tom H W K and Bokor J 1992 *Phys. Rev.* B **46** 13592
[75] Del Fatti N, Bouffanais R, Vallée F and Flytzanis C 1998 *Phys. Rev. Lett.* **81** 922
[76] Anisimov S I, Kapeliovich B L and Perel'man T L 1974 *Sov. Phys.—JETP* **39** 375
[77] Hirori H, Tachizaki T, Matsuda O and Wright O B 2003 *Phys. Rev.* B **68** 113102
[78] Groeneveld R H M, Sprik R and Lagendijk A 1995 *Phys. Rev.* B **51** 11433
[79] Wright O B and Kawashima K 1992 *Phys. Rev. Lett.* **69** 1668
[80] Wright O B 1994 *Phys. Rev.* B **49** 9985
[81] Bozovic I, Schneider M, Xu Y, Sobolewski R, Ren Y H, Lüpke G, Demsar J, Taylor A J and Onellion M 2004 *Phys. Rev.* B **69** 132503
[82] Bovensiepen U 2007 *J. Phys.: Condens. Matter* **19** 083201
[83] Melnikov A, Povolotskiy A and Bovensiepen U 2008 *Phys. Rev. Lett.* **100** 247401
[84] Hase M, Ishioka K, Demsar J, Ushida K and Kitajima M 2005 *Phys. Rev.* B **71** 184301
[85] Kaganov M I, Lifshitz I M and Tanatarov L V 1957 *Sov. Phys.—JETP* **4** 173
[86] Allen P B 1987 *Phys. Rev. Lett.* **59** 1460
[87] Demsar J, Averitt R D, Ahn K H, Graf M J, Trugman S A, Kabanov V V, Sarrao J L and Taylor A J 2003 *Phys. Rev. Lett.* **91** 027401
[88] Ahn K H, Graf M J, Trugman S A, Demsar J, Averitt R D, Sarrao J L and Taylor A J 2004 *Phys. Rev.* B **69** 045114
[89] Perfetti L, Loukakos P A, Lisowski M, Bovensiepen U, Berger H, Biermann S, Cornaglia P S, Georges A and Wolf M 2006 *Phys. Rev. Lett.* **97** 067402
[90] Kirchman P S 2009 Ultrafast electron dynamics in low-dimentional materials *PhD Thesis* Free Univ. Berlin

[91] Rettig L, Kirchmann P S and Bovensiepen U 2009 in preparation
[92] Eesley G L 1983 *Phys. Rev. Lett.* **51** 2140
[93] Schoenlein R W, Lin W Z, Fujimoto J G and Eesley G L 1987 *Phys. Rev. Lett.* **58** 1680
[94] Kabanov V V, Demsar J, Podobnik B and Mihailovic D 1999 *Phys. Rev.* B **59** 1497
[95] Spataru C D, Cazalilla M A, Rubio A, Benedict L X, Echenique P M and Louie S G 2001 *Phys. Rev. Lett.* **87** 246405
[96] Dresselhaus M S and Dresselhaus G 1982 *Light Scattering in Solids III* (*Topics in Applied Physics*) vol 51, ed M Cardona and G Güntherodt (Berlin: Springer) chapter 2
[97] Piscanec S, Lazzeri M, Mauri F, Ferrari A C and Robertson J 2004 *Phys. Rev. Lett.* **93** 185503
[98] Tangney P and Fahy S 1999 *Phys. Rev. Lett.* **82** 4340
[99] Fahy S and Reis D A 2004 *Phys. Rev. Lett.* **93** 109701
[100] Murray E D, Fritz D M, Wahlstrand J K, Fahy S and Reis D A 2005 *Phys. Rev.* B **72** 060301R
[101] Hase M, Kitajima M, Nakashima S I and Mizoguchi K 2004 *Phys. Rev. Lett.* **93** 109702
[102] Kolomenskii A A, Jerebtsov S N, Liu H, Zhang H, Ye Z, Luo Z, Wu W and Schuessler H A 2008 *J. Appl. Phys.* **104** 103110
[103] Zijlstra E S, Tatarinova L L and Garcia M E 2006 *Phys. Rev.* B **74** 220301R
[104] Kampfrath T, Perfetti L, Schapper F, Frischkorn C and Wolf M 2005 *Phys. Rev. Lett.* **95** 187403
[105] Saito R, Dresslhaus G and Dresselhaus M S 1998 *Physical Properties of Carbon Nanotubes* (Singapore: World Scientific)
[106] Sasaki K-I, Saito R, Dresselhaus G, Dresselhaus M S, Farhat H and Kong J 2008 *Phys. Rev.* B **77** 245441
[107] Wang Y, Kempa K, Kimball B, Carlson J B, Benham G, Li W Z, Kempa T, Rybczynski J, Herczynski A and Ren Z F 2004 *Appl. Phys. Lett.* **85** 2607
[108] Schultz H and Hüfner S 1976 *Solid State Commun.* **20** 827
[109] Debernardi A 2000 *Solid State Commun.* **113** 1
[110] Dresselhaus M S, Dresselhaus G, Saito R and Jorio A 2005 *Phys. Rep.* **409** 47
[111] Yee K J, Lim Y S, Dekorsy T and Kim D S 2001 *Phys. Rev. Lett.* **86** 1630
[112] Yee K J, Lee K G, Oh E, Kim D S and Lim Y S 2002 *Phys. Rev. Lett.* **88** 105501
[113] Loudon R 2001 *Adv. Phys.* **50** 813
[114] Gommans H H, Alldredge J W, Tashiro H, Park J, Magnuson J and Rinzler A G 2000 *J. Appl. Phys.* **88** 2509
[115] Scott J F 1974 *Rev. Mod. Phys.* **46** 83
[116] Akimov I A, Sirenko A A, Clark A M, Hao J-H and Xi X X 2000 *Phys. Rev. Lett.* **84** 4625
[117] Ma H, Kim W-J, Horwitz J S, Kirchoefer S W and Levy J 2003 *Phys. Rev. Lett.* **91** 217601
[118] Fahy S and Merlin R 1994 *Phys. Rev. Lett.* **73** 1122
[119] Wiederrecht G P, Dougherty T P, Dhar L, Nelson K A, Leaird D E and Weiner A M 1995 *Phys. Rev.* B **51** 916
[120] Brinc R and Zeks B 1974 *Soft Modes in Ferroelectrics and Antiferroelectrics* (Amsterdam: North-Holland)
[121] Dougherty T P, Wiederrecht G P, Nelson K A, Garrett M H, Jensen H P and Warde C 1992 *Science* **258** 770
Dougherty T P, Wiederrecht G P, Nelson K A, Garrett M H, Jensen H P and Warde C 1994 *Phys. Rev.* B **50** 8996
[122] Hase M, Kitajima M, Nakashima S and Mizoguchi K 2003 *Appl. Phys. Lett.* **83** 4921
[123] Kohmoto T, Tada K, Moriyasu T and Fukuda Y 2006 *Phys. Rev.* B **74** 064303
[124] Lu R, Hase M, Kitajima M, Nakashima S and Sugai S 2007 *Phys. Rev.* B **75** 012107
[125] Cavalleri A, Dekorsy Th, Chong H H W, Kieffer J C and Schoenlein R W 2004 *Phys. Rev.* B **70** 161102
[126] Kübler C, Ehrke H, Huber R, Lopez R, Halabica A, Haglund R F and Leitenstorfer A 2007 *Phys. Rev. Lett.* **99** 116401
[127] Okuda M, Naito H and Matsushita T 1992 *Japan. J. Appl. Phys.* 1 **31** 466
[128] Steigmeier E F and Harbeke G 1970 *Solid State Commun.* **8** 1275
[129] Cochran W 1959 *Phys. Rev. Lett.* **3** 412
[130] Rabe K M and Joannopoulos J D 1987 *Phys. Rev.* B **36** 6631
[131] Cummins H Z and Levanyuk A P 1983 *Light Scattering Near Phase Transition* (Amsterdam: North-Holland)
[132] Weiner A M, Leaird D E, Wiederrecht G P and Nelson K A 1990 *Science* **247** 1317
[133] Hase M, Itano T, Mizoguchi K and Nakashima S 1998 *Japan. J. Appl. Phys.* **37** L281
[134] Kim J-H, Han K-J, Kim N-J, Yee K-J, Lim Y-S, Sanders G D, Stanton C J, Booshehri L G, Hároz E H and Kono J 2009 *Phys. Rev. Lett.* **102** 037402
[135] Watanabe K, Takagi N and Matsumoto Y 2005 *Phys. Chem. Chem. Phys.* **5** 2697
[136] Yamada N, Ohno E, Nishiuchi K and Akahira N 1991 *J. Appl. Phys.* **69** 2849
[137] Yamada N and Matsunaga T 2000 *J. Appl. Phys.* **88** 7020
[138] Hegedüs J and Elliott S R 2008 *Nat. Mater.* **7** 399
[139] Sun Z, Zhou J and Ahuja R 2006 *Phys. Rev. Lett.* **96** 055507
[140] Sun Z, Zhou J and Ahuja R 2007 *Phys. Rev. Lett.* **98** 055505
[141] Kolobov A V, Fons P, Frenkel A I, Ankudinov A L, Tominaga J and Uruga T 2004 *Nat. Mater.* **3** 703
[142] Kolobov A V, Haines J, Pradel A, Ribes M, Fons P, Tominaga J, Katayama Y, Hammouda T and Uruga T 2006 *Phys. Rev. Lett.* **97** 035701
[143] Baker D A, Paesler M A, Lucovsky G, Agarwal S C and Taylor P C 2006 *Phys. Rev. Lett.* **96** 255501
[144] Andrikopoulos K S, Yannopoulos S N, Kolobov A V, Fons P and Tominaga J 2007 *J. Phys. Chem. Solids* **68** 1074
[145] Chong T C, Shi L P, Wei X Q, Zhao R, Lee H K, Yang P and Du A Y 2008 *Phys. Rev. Lett.* **100** 136101
[146] Tominaga J, Fons P, Kolobov A, Shima T, Chong T C, Zhao R, Lee H K and Shi L 2008 *Japan. J. Appl. Phys.* **47** 5763
[147] Lee B-S, Abelson J R, Bishop S G, Kang D-H, Cheong B-K and Kim K-B 2005 *J. Appl. Phys.* **97** 093509
[148] Först M, Dekorsy T, Trappe C, Laurenzis M, Kurz H and Béchevet B 2000 *Appl. Phys. Lett.* **77** 1964
[149] Hase M, Miyamoto Y and Tominaga J 2009 *Phys. Rev.* B **79** 174112
[150] Tomeljak A, Schäfer H, Städter D, Beyer M, Biljakovic K and Demsar J 2009 *Phys. Rev. Lett.* **102** 066404
[151] Burch K S, Chia E E M, Talbayev D, Sales B C, Mandrus D, Taylor A J and Averitt R D 2008 *Phys. Rev. Lett.* **100** 026409
[152] Sokolowski-Tinten K, Blome C, Blums J, Cavalleri A, Dietrich C, Tarasevitch A, Uschmann I, Förster E, Kammler M, Horn-von-Hoegen M and von der Linde D 2003 *Nature* **422** 287
[153] Cavalleri A, Wall S, Simpson C, Statz E, Ward D W, Nelson K A, Rini M and Schoenlein R W 2006 *Nature* **442** 664
[154] Nakamura K G, Ishii S, Ishitsu S, Shiokawa M, Takahasi H, Dhamalingam K, Irisawa J, Hironaka Y, Ishioka K and Kitajima M 2008 *Appl. Phys. Lett.* **93** 061905
[155] Dumitrica T, Garcia M E, Jeschke H O and Yakobson B I 2006 *Phys. Rev.* B **74** 193406
[156] Jeschke H O, Romero A H, Garcia M E and Rubio A 2007 *Phys. Rev.* B **75** 125412
[157] Wang F, Dukovic G, Brus L E and Heinzs T F 2005 *Science* **308** 838
[158] Makino K, Hirano A, Shiraki K, Maeda Y and Hase M 2009 *Phys. Rev.* B **80** 245428